Citation: Álvaro, J.J., Lorenzo, S., Martínez-Benítez, B., Pieren, A. P., 2024. Late Ediacaran carbonate production and REE+Y signatures tracing redox conditions in a Cadomian retroarc basin, Central Iberian Zone, Spain. Geologica Acta, 22.5, 1-22.
DOI: 10.1344/GeologicaActa2024.22.5

geologica acta

Late Ediacaran carbonate production and REE+Y signatures tracing redox conditions in a Cadomian retroarc basin, Central Iberian Zone, Spain

J. Javier Álvaro[1] Saturnino Lorenzo[2] Blanca Martínez-Benítez[1,3] Agustín P. Pieren[3]

[1]Instituto de Geociencias (CSIC-UCM)
Dr. Severo Ochoa 7, 28040 Madrid, Spain. Álvaro E-mail: jj.alvaro@csic.es
Martínez-Benítez E-mail: blancm05@ucm.es

[2]Departamento de Ingeniería Geológica y Minera-IGeA, Universidad de Castilla-La Mancha
Manuel Meca 1, 13400 Almadén, Spain. E-mail: saturnino.lorenzo@uclm.es

[3]Facultad de Ciencias Geológicas, Universidad Complutense de Madrid
José Antonio Nováis 12, 28040 Madrid, Spain. E-mail: apieren@ucm.es

ABSTRACT

The late Ediacaran carbonate production recorded in a Cadomian retroarc basin from the Iberian Peninsula provides an excellent opportunity to evaluate the tectonic and redox factors that controlled the infill of the foredeep troughs, located between uplifted orogenic wedges and exposed forebulge transects. In the Central Iberian Zone of the Iberian massif, the carbonates of the Villarta Formation follow two geographic belts, which represent short-term mosaics of uplifted and tilted fault-bounded basement highs. These recorded the nucleation of fringing reefal (rich in *Cloudina* and *Sinotubulites* microfossils embedded in thromboid textures) and shoal and back-barrier complexes, which episodically fed slope-related megabreccia lobes and channels. REE+Y datasets from the impure carbonates reflect contamination by detrital material, hydrothermal interaction and variable redox conditions, ranging from oxic to dysoxic, the latter emphasized by the deposition of kerogenous black shales in distal parts of the foredeep trough.

KEYWORDS **Carbonate factory. Megabreccia. Ediacaran. Cadomian Retroarc basin. Gondwana.**

INTRODUCTION

Although carbonate production in arc to retroarc basins has so far not received enough attention compared to other carbonate reservoir topics, nucleation, growth and demise of carbonate factories is an important component monitoring the stratigraphic framework neighbouring arc settings (*e.g.* Catuneanu, 2004; Dorobek, 2007). Differential tectonic subsidence and uplift along convergent plate margins strongly control depocenter migration, driven by modifications in fault displacement and induced rates of accommodation space, as well as fluctuations in sediment flux overwhelming carbonate (microbial and shelly) productivity (DeCelles, 2012; Horton, 2022). In the case of the Cadomian arc to retroarc basins preserved in the Iberian Peninsula, the identification and lateral correlation of the short-term episodes of carbonate production is a puzzled task constrained by the severe Variscan tectonothermal

overprint that affected the Cadomian basement (Álvaro *et al.,* 2019a; Bandrés *et al.,* 2002; Díez Balda *et al.,* 1990; García-Hidalgo, 1985).

In retroarc basins, fault-bounded basement highs, episodically protected from terrigenous poisoning, may allow the development of carbonate factories throughout short-term narrow ramps and rimmed shelves flanked by fringing reefs, which are mainly influenced by the activity of fault networks accommodating stretching (Dorobek, 2007). As carbonate productivity is largely a function of nutrient availability (growth of photosynthesizing organisms depends on nutrient availability in water; *e.g.* Clavera-Gispert *et al.,* 2012; Coletti *et al.,* 2017) and increased organic production is a primary driver of marine anoxia (*e.g.* Liu *et al.,* 2018), two major antagonistic processes were selected for analysis in the Cadomian retroarc basin preserved in the Central Iberian Zone: carbonate production and redox conditions. Carbonate production is commonly suppressed by high nutrient levels, potentially controlled by i) intense chemical weathering of arc and proximal retroarc exposures and ii) upwelling of cold, nutrient-rich deep waters (Halfar *et al.,* 2004). In the Cadomian retroarc basin, the association of upper Ediacaran carbonates with black shales (Valladares, 1995; Valladares *et al.,* 2000) and phosphates (Álvaro *et al.,* 2016), punctuated by eutrophic episodes fed by cyanobacterial blooms of *Bavlinella* acritarchs (Álvaro *et al.,* 2024a; Palacios Medrano, 1989), point to the apparent coincidence of stagnant troughs with water stratification and open-sea, high-productivity, upwelling settings. The aims of this paper are: i) to review the upper Ediacaran, microbial and shelly, carbonate production recorded in the Central Iberian Zone of Spain; ii) to update the major diagenetic processes and to establish the redox conditions preserved in these carbonates, based on Rare Earth Element and Yttrium (REE+Y) geochemical features and iii) to understand the palaeogeographic interaction between carbonate production and microbial eutrophication tracing redox conditions preserved in these spotted Cadomian retroarc relics.

GEODYNAMIC SETTING AND STRATIGRAPHY

The Iberian massif, which roughly covers the western half of the homonymous peninsula, comprises a Precambrian–Palaeozoic complex mainly structured during the Cadomian and Variscan orogenic cycles. The Iberian massif is traditionally subdivided into several Variscan tectonostratigraphic units or zones (Lotze, 1945) (Fig. 1A). This paper focuses on the Central Iberian Zone, which preserves the relics of a Cadomian retroarc transect (Álvaro *et al.,* 2019a; Díez Balda *et al.,* 1990; San José *et al.,* 1992). Based on the style of Variscan deformation, two major structural sectors may be differentiated in the Central Iberian Zone, known as the domains of Recumbent and Vertical Folds (Fig. 1B). They traditionally correspond to the Castillian-Galician sub-zone to the NE and the Portuguese-Alcudian sub-zone to the SW, respectively, the former bearing abundant synorogenic granitoid bodies and higher grade of metamorphism (Lotze, 1945). Their contact is somewhat imprecise due to the large number of Variscan granitoid intrusions punctuating it. The Domain of Vertical Folds, on which this study focus, spreads throughout the southwestern contact with the Ossa-Morena Zone. It is characterized by a succession of NW–SE trending narrow synclines and larger anticlines comprising Ediacaran–Cambrian cores flanked by the Lower Ordovician Armorican Quartzite (Fig. 1B).

The Ediacaran–Terreneuvian lithostratigraphic nomenclature of the anticlines that belong to the Domain of Vertical Folds (Fig. 1B) is abundant, resulting from the mapping and lithostratigraphic subdivision of each anticlinal core. Recently, Álvaro *et al.* (2019a) proposed an integrated lithostratigraphic nomenclature for the Alcudia valley and the Toledo Mountains (Castilla-La Mancha and Extremadura regions), which is here extended to the Salamanca-Hurdes Dome (Castilla-León region; Rodríguez Alonso, 1984; Ugidos *et al.,* 2020).

The upper Ediacaran sedimentary bodies recorded in the Central Iberian Zone represent the stepwise infill of an asymmetric Cadomian retroarc depocenter. They display numerous wedge-shaped geometries punctuated by stratigraphic gaps, which are markedly different following (present-day) SW–NE trending shifts (Álvaro *et al.,* 2019a). A late Cadomian kilometre-scale folding event (Álvaro *et al.,* 2019b; Pieren Pidal, 2009; Pieren Pidal *et al.,* 1991; San José *et al.,* 1992), lacking associated cleavage and metamorphism, is inferred as responsible for the distinct gap that separates two major megasequences belonging to the traditional Schist-Greywacke Complex (Carrington da Costa, 1950): i) the Lower Alcudian-Domo Extremeño Supergroup (with topmost part dated at 565±4Ma; Linnemann *et al.,* 2018) and ii) the Cíjara Formation and lateral equivalent Ibor Group (the lower part of the latter dated at 560±2Ma; Álvaro *et al.,* 2024b). The end of retroarc geodynamic conditions is stratigraphically marked by another major unconformity, interpreted as a Cadomian orogenic collapse, overlain by upper Fortunian chaotic megabreccias (*e.g.* Fuentes, Membrillar and Navalpino beds) and conglomerates (San Lorenzo Formation) recording the first rift-related magmatic pulses (Álvaro and Lorenzo, 2022; Rodríguez Alonso *et al.,* 2004).

The only episode of carbonate production recognized throughout this thick succession is found in the Ibor Group and its Portuguese counterpart, the black graphitic slates with marble interbeds of the Bateiras Formation (Douro

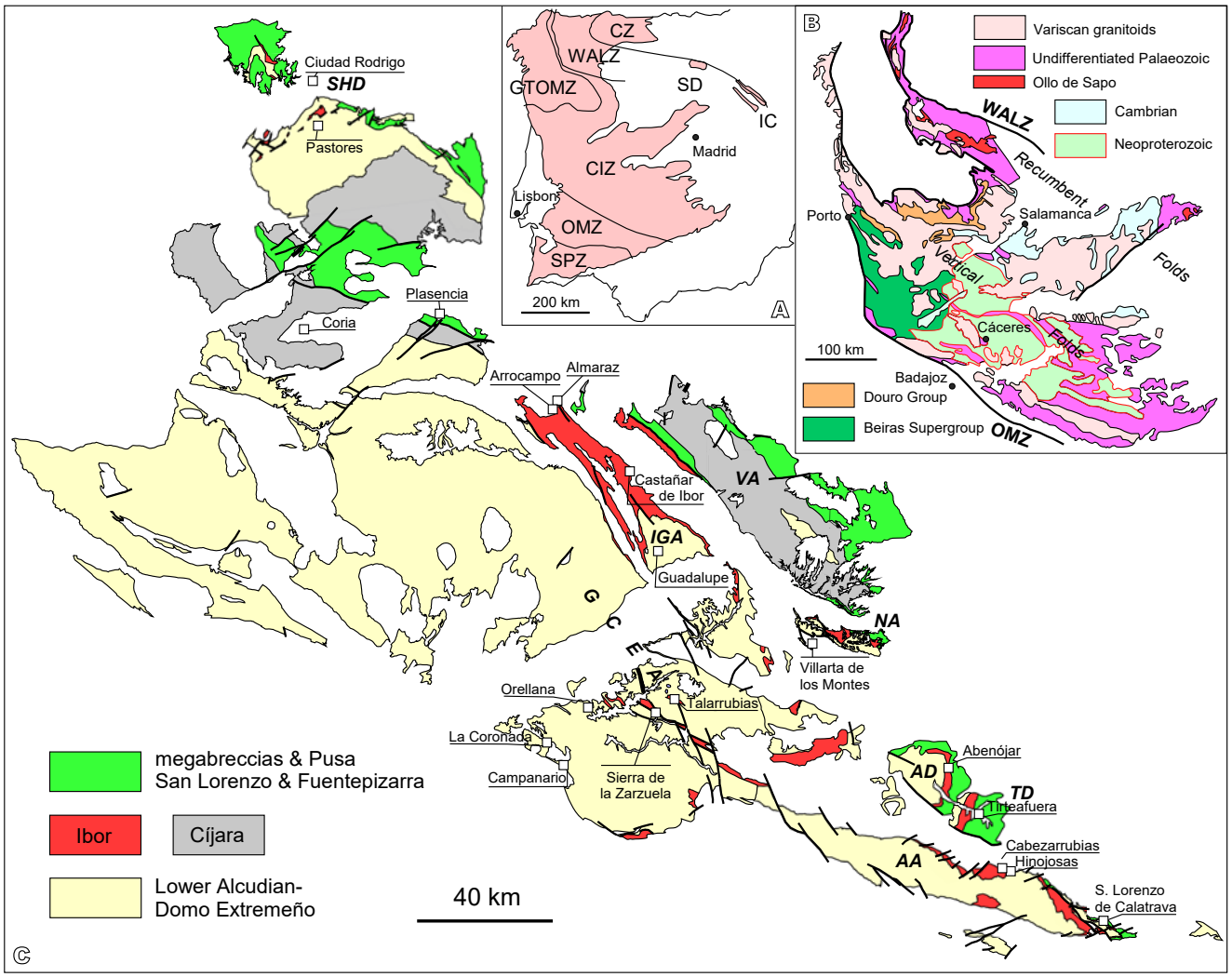

FIGURE 1. A) Geographical distribution of the Iberian massif with Variscan zones . B) Geological sketch of the Central Iberian Zone, Iberian Massif. C) Geological map of the Ediacaran–Terreneuvian basement from the Central Iberian Zone in Spain; based on de San José (1984), Rodríguez Alonso (1984), de San José *et al.* (1992), López Díaz (1995), Pieren Pidal (2000), Palacios *et al.* (2010) and Meireles *et al.* (2013). Abbreviations: AA= Alcudian Anticline, AD= Abenójar Dome, CZ= Cantabrian Zone, CIZ= Central Iberian Zone, GCEA= Great Central Extremenian Anticlinorium, GTOMZ= Galicia-Trás-Os-Montes Zone, IC= Iberian Chains, IGA= Ibor-Guadalupe Anticline, NA= Navalpino Anticline, OMZ= Ossa-Morena Zone, SD= Sierra de la Demanda, SHD= Salamanca-Hurdes Dome, SPZ= South Portuguese Zone, TD= Tirteafuera Dome, VA= Valdelacasa Anticline and WALZ= West Asturian-Leonese Zone.

Group; Meireles *et al.,* 2013). In the Central Iberian Zone, the outcrops of the Ibor Group and the Bateiras Formation follow two geographic belts separated by exposures of the penecontemporaneous siliciclastic-dominant Cíjara Formation and its laterally equivalent in Portugal, the Caneiro Formation (Lousã Group, Beiras Supergroup; Medina *et al.,* 1998; Sequeira, 2011; Fig. 2). The outcrops of the Ibor Group are mainly exposed in the Sierra de la Zarzuela and the shoreline of the Orellana dam (Great Central Extremenian Anticlinorium, GCEA), the Ibor-Guadalupe, Navalpino and Alcudia anticlines, and the Salamanca-Hurdes, Abenójar and Tirteafuera domes (Figs. 1C–2). The group is subdivided, from bottom to top, into the Castañar, Villarta and Arrocampo formations.

The Castañar Formation, up to 400m thick, is characterized by conglomerates and subsidiary breccia lenses, rich in heterolithic (carbonate-free) clasts, capped by sandstones and shales locally punctuated by dolostone layers and nodules. The shale interbeds contain vendotaenids, simple horizontal ichnofossils, and club and spindle-shaped carbonaceous remains (Hufnagel, 2008; Jensen and Palacios, 2016; Palacios *et al.,* 2010). The formation has been interpreted as the infill of an inherited palaeotopography, with slope-related and alluvial to fluvial environments finally succeeded by marine nearshore sediments (Álvaro *et al.,* 2019a; Palacios *et al.,* 2010; Pieren Pidal *et al.,* 1991).

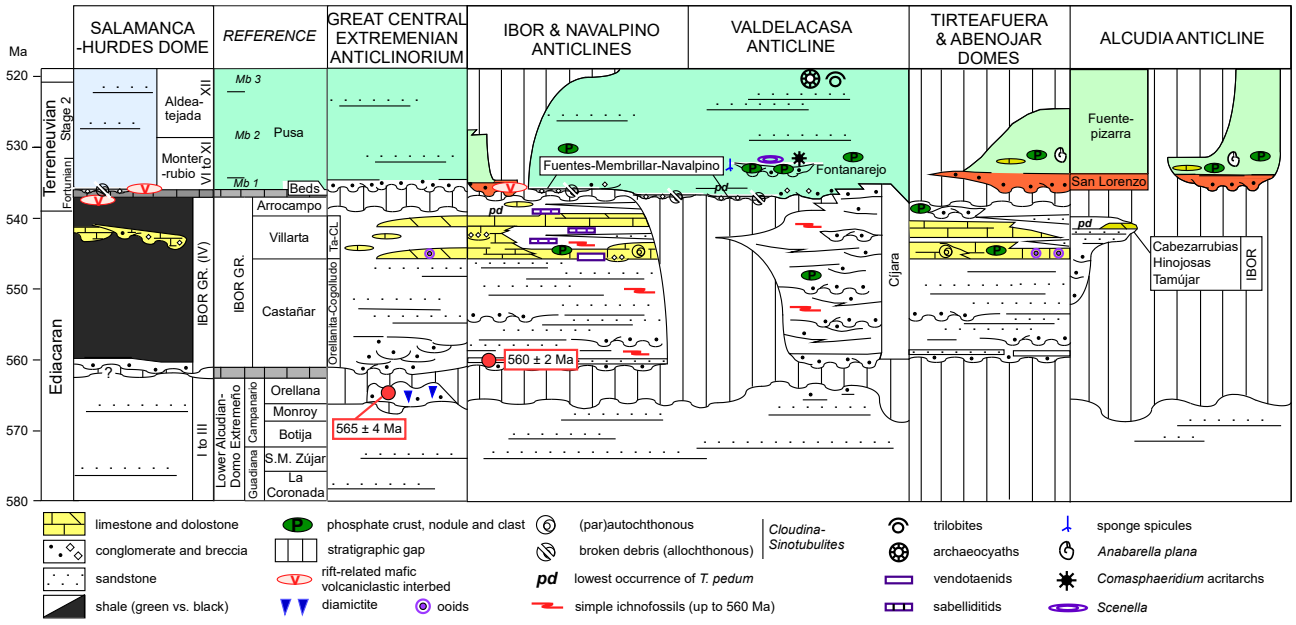

FIGURE 2. Stratigraphic framework of the Ediacaran–Cambrian transition throughout the Central Iberian Zone in Spain; based on Rodríguez-Alonso (1984), Palacios Medrano (1989), Díez Balda *et al.* (1990), Pieren Pidal (2000), Rodríguez-Alonso *et al.* (2004), Álvaro *et al.* (2016, 2019a, 2020a, 2024b, c), Valladares *et al.* (2000), Jensen and Palacios (2016), Linnemann *et al.* (2018), Ugidos *et al.* (2020), Álvaro and Lorenzo (2022), and references therein. Abbreviation: Ta-CL= Talarrubias and Collado de la Liebre units. Radiometric ages: 565 ± 4Ma (U–Pb LA–SF–ICP–MS on zircon; Linnemann *et al.*, 2018) and 560 ± 2Ma (SHRIMP, CA-ID-TIMS and CA-SHRIMP on zircon; Álvaro *et al.*, 2024b).

The heterolithic Villarta Formation, up to 250m thick (Figs. 1C–3), exhibits sharp lateral changes in facies and thickness. Shelly-microbial buildups from the Ibor-Guadalupe and Navalpino anticlines contain *Cloudina* and *Sinotubulites* shelly debris (Álvaro *et al.*, 2020a; Cortijo *et al.*, 2010, 2015). Some shale interbeds have yielded vendotaenids, sabelliditids and simple treptichnid ichnofossils.

The Arrocampo Formation conformably overlies the Villarta Formation. It is a shale-dominated unit, up to 350m thick, with subsidiary sandstone interbeds and scattered centimetre-scale carbonate nodules. The ichnofossil *Treptichnus pedum* has been reported from the basal part of the formation so tentatively marking the base of the Fortunian (Álvaro *et al.*, 2019a; Jensen and Palacios, 2016; Simón, 2018). The Arrocampo Formation is capped by the pre-rift unconformity (Álvaro and Lorenzo, 2022).

In the Alcudia Anticline, the same lithostratigraphic triad of the Ibor Group has been traditionally subdivided into the Tamujar, Hinojosas and Cabezarrubias formations (Pieren Pidal, 2000, 2009) (Figs. 2–3). Some thin shale interbeds within the carbonate-dominant Hinojosas Formation has yielded treptichnids and *Monomorphichnus* isp. (García-Hidalgo, 1985), but the first distinct specimens of *T. pedum* occur in the basal centimetres of the overlying Cabezarrubias Formation (Álvaro *et al.*, 2024b). Based on U–Pb detrital zircon analysis, Talavera *et al.* (2015) established a maximum gap for the Lower Alcudian-Domo Extremeño/Tamujar unconformity of about 28m.y., bracketed between 580–576Ma and 555–552Ma estimates, respectively. In a similar way, the same lithostratigraphic triad can be also recognized in the surroundings of the Sierra de la Zarzuela (GCEA), where Pieren Pidal (2000) distinguished: i) the Orellanita conglomerates and the Cogolludo Sandstone, ii) the Talarrubias Dolostone and the Collado de la Liebre sandstone/shale alternations and top dolostone and iii) some unnamed shales and calcschists (Figs. 2–3).

Finally, one informal lithostratigraphic unit or sequence, labelled IV by Valladares *et al.* (2000) and bounded by two unconformities, is the lateral equivalent of the Villarta Formation in the Salamanca-Hurdes Dome. The formation there, up to 500m thick, includes: i) a lower unit of massive to laminated black shales, locally capped by ii) a mixed carbonate-siliciclastic slope-apron lenticular deposit, up to 260m thick and 3km long, finally onlapped by iii) a black shale unit (Valladares, 1995; Valladares *et al.*, 2000). The topmost part of the group is scoured by megabreccias (level V) comprising limestone boulders that contain allochthonous debris of *Cloudina* (Díez Balda *et al.*, 1990; Vidal *et al.*, 1994).

MATERIAL AND METHODS

Several stratigraphic logs were measured and sampled in the Alcudia, Navalpino and Ibor-Guadalupe anticlines, the GCEA, and the Abenójar, Tirteafuera and Salamanca-Hurdes domes of the Central Iberian Zone, Spain (Fig. 1B). Thin-sections of carbonate samples, stained with Potassium Ferricyanide and Alizarin Red S, were petrographically characterized by transmitted light microscopy, Scanning Electron Microscopy (SEM; at Museo Nacional de Ciencias Naturales, Madrid) operating in Back-Scattered Electron (BSE) image and Energy Dispersive X-ray (EDS) analysis, and separate cold Cathodoluminescence microscopy (CL; at Instituto Geológico y Minero de España, Tres Cantos). Analytical results of BSE and EDS display an error of ±5 to 7%.

Geochemical data of selected impure limestone and dolostone samples are based on 25 chemical analyses. The major, trace and rare earth elements were analyzed using X-ray fluorescence and Inductively Coupled Plasma Mass Spectrometry (ICP-MS) at AcmeLabs, Canada, where the accuracy for major, trace and rare elements is currently less than 2, 5–10 and 3–7%, respectively.

The REE+Y patterns were normalized to the Post-Archaean Australian Shale standard (PAAS; Pourmand *et al.*, 2012). Light-to-heavy fractions were estimated with the Pr(SN)/Yb(SN) ratio. True negative Ce(SN) anomalies display Ce/Ce* [=Ce(SN)/(0.5(Pr(SN)+La(SN))] and Pr/Pr* [=Pr(SN)/(0.5Ce(SN)+0.5Nd(SN))] values less than and greater than unity, respectively. Such an approach discriminates between positive La(SN) and true negative Ce(SN) anomalies (Bau and Dulski, 1996; Planavsky *et al.*, 2010). Present-day marine oxygenated settings show significant negative Ce(SN) anomalies when normalized to PAAS, whereas suboxic and anoxic waters lack it (Byrne and Sholkovitz, 1996). Eu anomalies are calculated as

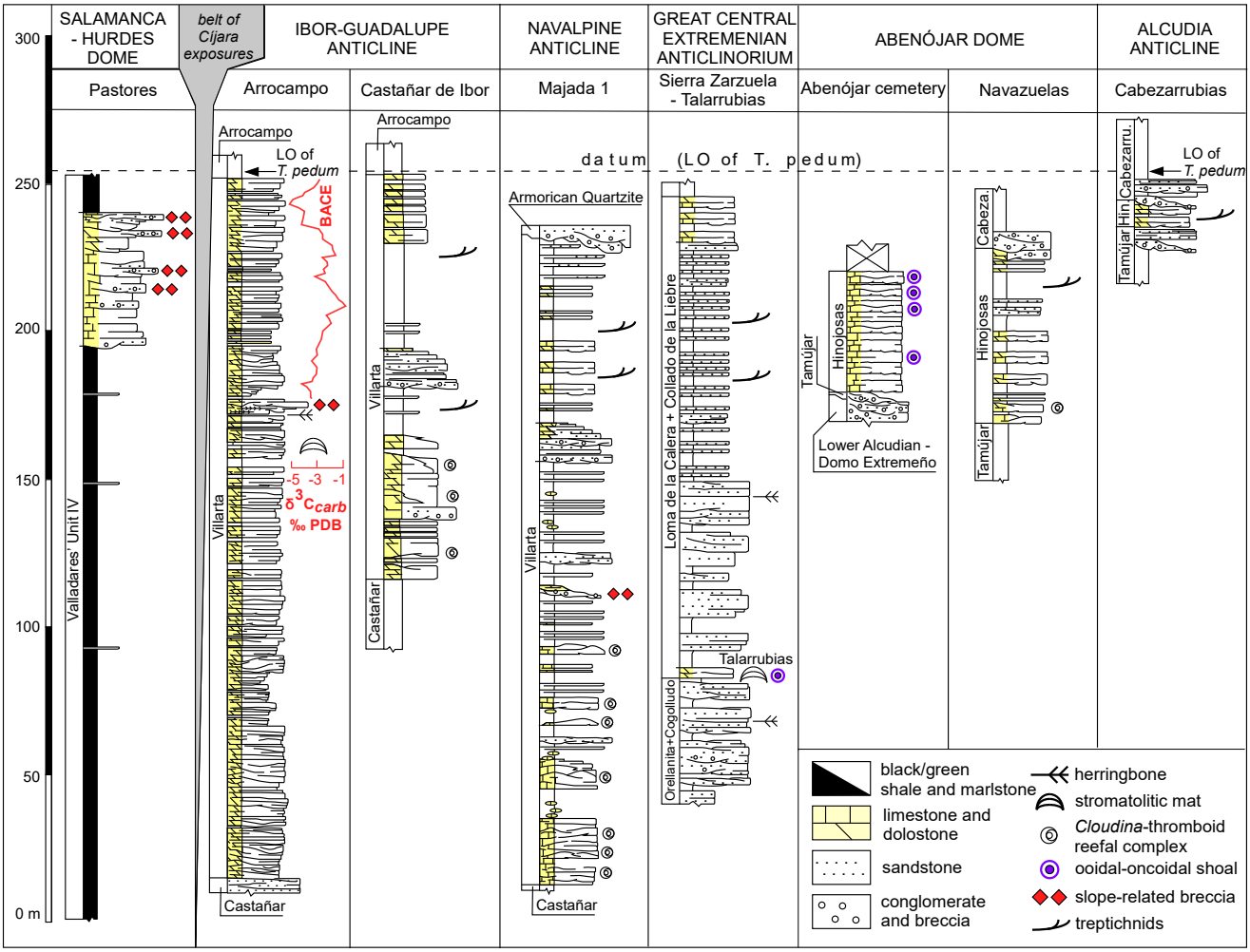

FIGURE 3. Simplified stratigraphic logs reported in the text showing main facies associations and significant sedimentary structures; LO= Lowest Occurrence; chemostratigraphic shift of the Basal Cambrian Carbon Isotope Excursion (BACE), after Álvaro *et al.* (2024b).

Eu/Eu* [=Eu(SN)/(0.66Sm(SN)+0.33Tb(SN))]. Yttrium displays an inverse behaviour of light Rare Earth Elements (REE) and Ce in redox-stratified basins, favouring Y/Ho values > PAAS ratios for marine environments. As a result, suboxic and anoxic waters commonly lead to a decrease in dissolved seawater Y/Ho ratios (Bau and Dulski, 1996).

CARBONATE FACIES ASSOCIATIONS AND ENVIRONMENTS

The representative stratigraphic sections of the above-reported tectonostratigraphic units are illustrated in Figure 3, and their facies associations summarized in Table 1. They are reported below following a SE to NW (present coordinates) trend.

Alcudia Anticline

The Alcudia Anticline is a Variscan structure, about 130km long and striking WNW–ESE. Its core is formed by Ediacaran to Terreneuvian strata. The Hinojosas Formation is well exposed in the vicinity of the homonymous and Cabezarrubias villages (Fig. 1B). There, the formation, up to 9m thick, is composed of dolostone/shale alternations with subsidiary greywacke (Peláez *et al.,* 1988; Fig. 3). Although the original fabric and texture of the carbonates are locally overprinted by strong dolomitization, patchy fissuring (Fig. 4A) and hydrothermal veining (Fig. 4B), some dolostone beds display parallel, low-angle and crinkled laminae, locally scoured by sets with trough cross-stratified stratification. The erosive base of the overlying Cabezarrubias Formation is capped by lenticular conglomerates and coarse-grained litharenites. Their infill consists of clast-supported textures rich in quartzite, vein quartz, shale, ferruginized dolostone and phosphate clasts, bearing fissuring and veining networks occluded by iron oxyhydroxides, and pure hematite/goethite and chert clasts (Fig. 4C–D). Some interlaminae are emphasized by millimetre-thick phosphatic crusts.

Carbonate laminations and scouring relationships reflect development of decimetre-scale stromatolites, as well as lenticular carbonate shoals embedded in green shales (Pieren Pidal, 2000). The base of the overlying Cabezarrubias Formation is marked by channels and shoal complexes scouring the Hinojosas top. They contain polyphase clasts displaying the fissuring and hydrothermal

TABLE 1. Summary of the representative facies associations reported in the text

ENVIRONMENTS	LITHOLOGY, FABRICS AND TEXTURES	LOCATION
low-energy peritidal carbonates punctuated by storm-induced episodes	fenestral lime mudstones, microbial laminites, and low-angle to parallel-laminated and ripple cross-laminated sparry +peloidal packstones	upper sequence at Arrocampo, upper member at Castañar de Ibor
wavy-bedded peritidal to foreshore carbonates	wavy to nodular bedded peloidal packstones, with parallel, lenticular wavy and nodular bedding alternating with planar and cross-laminae punctuated by scoured surfaces	upper sequence at Arrocampo, upper member at stratotype and Castañar de Ibor
high-energy, carbonate sand shoal complex	peloidal-ooidal-oncoidal-intraclastic packstones to grainstones with concentric cortices, sparry crystals and peloids as nuclei, and arranged in parallel to cross-stratified sets, with scarce bimodal herringbone interbeds	lower sequence at Arrocampo, lower member at Abenójar and both members at Sierra de la Zarzuela-Talarrubias and Cabezarrubias
Cloudina-thromboid reef complexes	coalesced patch-reefs and biostromes forming massive build-up complexes, surrounded by reef-derived slope breccias, alternating with inter-reef, shelly packstone to wackestone and shaly beds	lower member at stratotype, Navazuelas and Castañar de Ibor
mixed fringing slopes	gravity-driven and slope-collapse structures, such as slump folds and olistostromes, matrix-rich boulder breccias, truncation of deformation structures, and liquefaction and fluidification of unconsolidated beds	lower member at stratotype, middle member at Pastores and marking discontinuity at Arrocampo
mixed shoaling complexes	shales to poorly to well-sorted litharenites, with intergranular pores occluded with carbonate cements, amalgamated as coarsening- and thickening-upward cycles rich in cross-stratified sets and scouring surfaces	middle member at stratotype, Castañar de Ibor, Sierra de la Zarzuela, Navazuelas and Cabezarrubias
mixed conglomeratic channels	sand to cobble, polymictic conglomerates with significant proportion of carbonate intraclasts and matrix	middle member at stratotype, Castañar de Ibor, Sierra de la Zarzuela, Navazuelas and Cabezarrubias

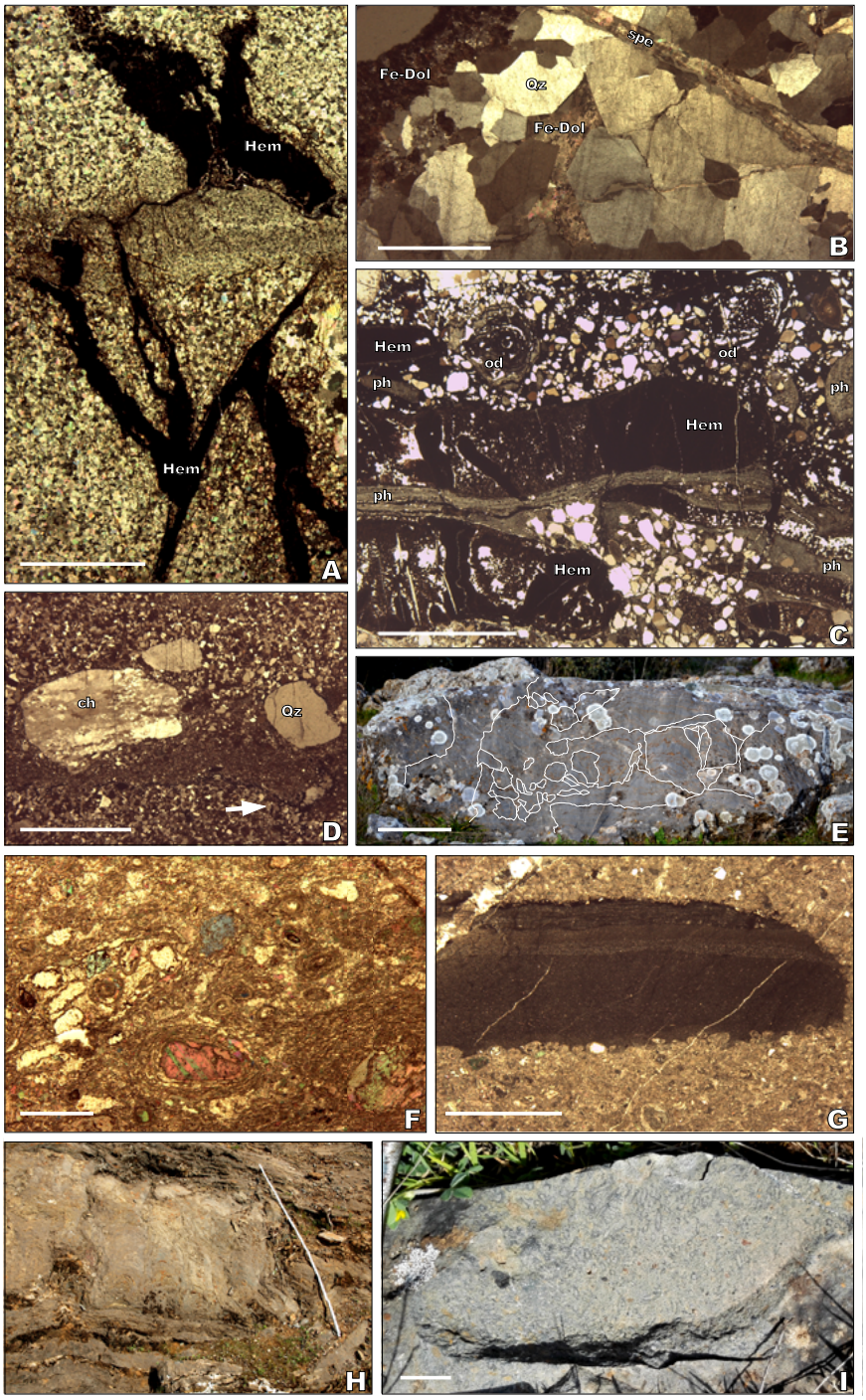

FIGURE 4. Representative sedimentary bodies and petrographic features of the Hinojosas Formation in the Alcudia Anticline, and the Villarta Formation in the Abenójar Dome and Navalpino Anticline. A) Fissuring and veining of microsparry to sparry dolomitic alternation, occluded with iron oxyhydroxides, and subsequently affected by late diagenetic stylolites and solution seams; Cabezarrubias log, scale bar= 5mm. B) Mosaics of vein quartz crosscutting a previously dolomitized host-rock, subsequently affected by a fissure occluded by a Quaternary karstic speleothem; Hinojosas stratotype; scale bar= 5mm. C) Conglomeratic channel marking the base of the Cabezarrubias Formation at its homonymous stratotype, rich in pebble-to cobble-sized, ironstone, chert and phosphatic clasts, locally encrusted by phosphatic laminae, and scattered hematite ooids; scale bar= 5mm. D) Cobble-sized clasts of vein quartz and chert forming a lag embedded in the Hinojosas stratotype (erosive surface arrowed); scale bar= 5mm. E) Topmost part of the Villarta Formation in the Navazuelas stream, Abenójar Dome, with marked outlines of a synsedimentary brecciated fabric affected by subvertical fissuring; scale bar= 20cm. F) Recrystallized ooidal-oncoidal grainstone (allochems with sparry cores) from the log neighbouring the Abenójar cemetery; scale bar= 1mm. G) Another detail of the former grainstone showing the presence of exotic laminated black shale clasts; scale bar= 5mm. H) Lateral edge of a *Cloudina*-microbial patch-reef (see distinct columnar stromatolites growing from the base) onlapped by marly flanks from the lower member of the Villarta stratotype; scale= 1m. I) Detail of a fragmented slab from a reefal core showing oblique sections of *Cloudina* shells; scale= 2cm. Abbreviations: Fe-Dol= Fe-Dolomite, Hem= Hematite, od= ooid, ph= phosphate, Qz= Quartz, spe= speleothem.

processes that affected the underlying carbonate levels, as well as penecontemporaneous phosphogenetic processes.

Tirteafuera and Abenójar domes

The shape of these NW–SE trending domes is constrained by the interference of two Variscan deformation phases broadly exhibiting perpendicular orientations. Their cores comprise the Lower Alcudian-Domo Extremeño Supergroup, the Ibor Group and Terreneuvian formations (Fig. 1B). Two representative logs were measured and sampled to illustrate their lithological and facial features, in the vicinity of the Abenójar cemetery and along the Navazuelas stream to the north (Figs. 2B; 3). The former log, about 40m thick, unconformably overlies some chaotic megabreccias (known regionally as "disorganized facies") belonging to the Lower Alcudian-Domo Extremeño Supergroup, whereas its top is faulted (Calvet and Salas, 1988; Lorenzo Álvarez and Solé, 1988). Carbonate and mixed strata display a lower massive to bedded package of grey limestones with variable abundances (up to 30% in volume) of silty and sandy impurities, mainly quartz, feldspar, chert and muscovite flakes with scattered peloids and oncoids. The upper part consists of limestone/shale alternations with decimetre-scale lenses of sparry ooidal-oncoidal packstones, rich in concentric allochems with sparry cores (Fig. 4F) and exotic black shale clasts (Fig. 4G), locally interrupted by bedded dolostone interbeds.

In contrast, the Navazuelas stream log exhibits a complete succession of the Villarta Formation, about 250m thick, mirroring the threefold subdivision recorded in the Navalpino and Ibor-Guadalupe anticlines (see below). The lower member comprises limestone/shale couplets where bedded to plano-convex and lenticular shapes, outlined by stromatolitic crusts, can be identified. Simón (2018) illustrated some conical microfossils interpreted as poorly preserved specimens of *Cloudina*. The second member consists of amalgamated cross-stratified to bedded sets of sandstone. The upper member shows the return to limestone/shale alternations, where some limestone interbeds are fissured and brecciated (Fig. 4E). Their breccia clasts also occur infilling some overlying scouring lenticular sets.

Although incomplete, the Abenójar cemetery log illustrates the record of ooidal-oncoidal shoal complexes sealing an inherited palaeorelief, composed of the Lower Alcudian-Domo Extremeño Supergroup, which yielded (exotic) black shale clasts. The neighbouring Navazuelas log shows the typical three-fold subdivision of the Villarta Formation, with development of (poorly preserved) *Cloudina* patch-reefs in the lower member, siliciclastic shoaling complexes in its middle member, and the final re-establishment of carbonate factories in the upper member. The latter consists of carbonate interbeds subsequently affected by fissuring and brecciation, reflecting renewed episodes of tectonic instability of the substrate.

Navalpino Anticline

The core of the asymmetrical Navalpino Anticline comprises both the Lower Alcudian-Domo Extremeño Supergroup and the unconformable Ibor Group, which together shaped a tilted palaeorelief unconformably overlain by Terreneuvian formations. The anticlinal core is unconformably flanked by strata of the Armorican Quartzite (Álvaro *et al.,* 2016; López Díaz, 1995; San José, 1984). The stratotype of the Villarta Formation (220m thick) lies to the north of the homonymous village, flanking the Cíjara dam and it is unconformably overlain by the Armorican Quartzite. Previously, it has been subdivided into three members, from bottom to top: i) bedded and lenticular carbonates encased in greenish shales; ii) conglomerates and sandstones grading upward to sandy dolostones and iii) couplets of bedded carbonates and shales (see details in Álvaro *et al.,* 2020a).

The lower member comprises, decimetric to metric, shelly-microbial patch, biohermal and complex reefs (Fig. 4H) embedded in monotonous shales rich in vendotaenids. Reefal cores comprise mesoclots of dense microbial microsparite containing *Cloudina* (Fig. 4I) and *Sinotubulites* assemblages (Cortijo *et al.,* 2010, 2015), separated by laminated (stromatolitic) fabrics. Reefal flanks contain gypsum pseudomorphs (Álvaro *et al.,* 2020a: fig. 10G–H). The easternmost outcrops exhibit chaotic breccia interbeds, up to 30cm thick, composed of unsorted, polymictic, pebble-to sand-sized clasts. The breccia beds are crosscut by steeply dipping veins and fissures, subsequently occluded by hematite, barite and dolomite cements (Álvaro *et al.,* 2020a) (Fig. 5A–B).

The middle member, about 12–16m thick, comprises an amalgamation of lenticular conglomerates and sandstones, grading upsection into sandy dolostones with shaly interbeds (Fig. 5C) rich in sabelliditids. Basal channels, 1.2m thick and up to 2.4m wide, are infilled by slightly calcareous (10–20% of dolomite miscrosparry cement), well-sorted, fine- to medium-grained subarkoses. Their bases are marked by subhorizontal to broadly concave-upward scoured surfaces. They are capped by lags, <20cm thick, of subangular to angular, goethite- to hematite-coated rip-up clasts, up to 12cm long, of dolostone and shale. Channel-fill structures display stacked, fining trends of small- to large-scale (each of them <1.4m thick), planar to through cross-stratified sets with local low-angle lamination. The palaeocurrents of channel axes mark an overall SW–NE direction. The whole amalgamated package forms a fining- and thinning-upward trend, consisting of sandy dolostones with siliciclastic content below 20%.

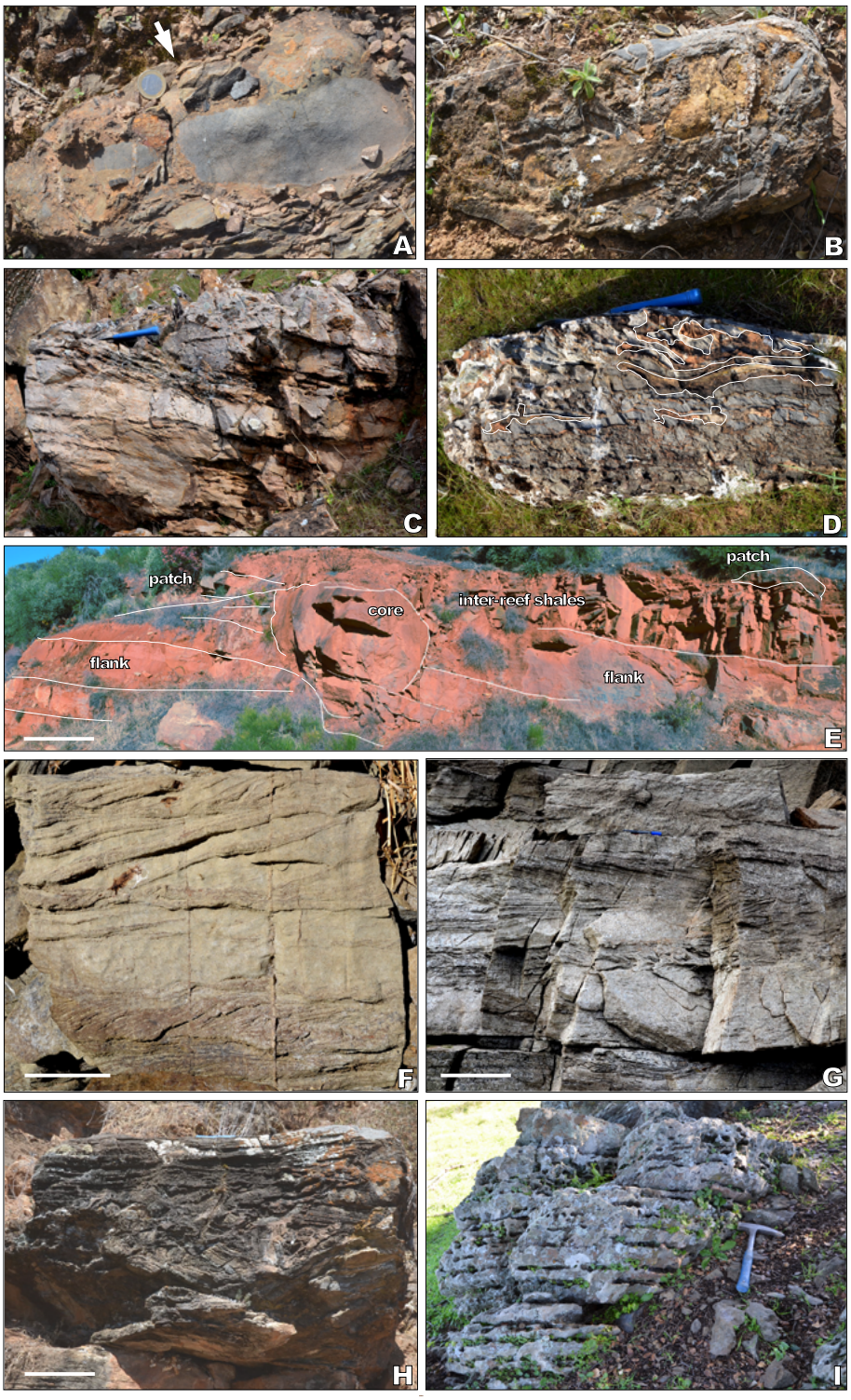

FIGURE 5. Representative sedimentary bodies of the Villarta Formation in the Navalpino and Ibor-Guadalupe anticlines and the Great Central Extremenian Anticlinorium. A–B) Breccia lenses, rich in limestone (grey) and dolostone (orange) clasts subsequently affected by hydrothermal quartz veining, interrupting the top of the lower member at the southeasternmost outcrop of the type area, north of Villarta de los Montes. C) Middle member of the Villarta Formation with superposition of multidirectional cross-stratified sets from the Villarta stratotype. D) Block from the upper member of the Villarta Formation at its stratotype showing a superposition of breccia limestone packages punctuated by orange-stained dolostone interbeds. E) Field view of the lower member in the vicinity of Castañar de Ibor exhibiting a wholly dolomitized, *Cloudina*-microbial reefal complex. F) Superposition of cross-stratified to low-angle laminated set of impure dolostones from the lower sequence of the Arrocampo log; scale bar= 10cm. G) Herringbone structures from the top of the lower sequence in Arrocampo; scale bar= 10cm. H) Breccia lens of boulder-sized dolostone and chert clasts separating two sequences at Arrocampo; scale bar= 20cm. I) Wavy to undulated beds of impure limestone from the Collado de la Liebre Bed, Sierra de la Zarzuela, GCEA.

Finally, the upper member comprises alternations of ribbon limestone to dolostone beds and shales. Ribbon carbonates display wavy to irregular- beds affected by dolomitization fronts crosscutting the stratification plane. In some cases, carbonate lenses are wholly brecciated and punctuated by dolomitized lenses (Fig. 5D). Carbonate/shale contacts are uneven to irregular, locally displaying load casts, hummocks and gutters. Shales comprise scattered simple ichnofossils.

The lower member represents shelly-microbial reefal nucleation and growth on clear water, low-energy substrates, at depths ranging between normal and storm wave base. The stromatolite and thrombolite buildups that shaped patch-reefs, biostromes and amalgamated reefs, developed on stable substrates. The margin of some syndepositional fault blocks are fringed by lobe complexes composed of polyphasic, clast-supported breccias. Their clasts derived from the above-reported reefs mixed with exotic phosphatic clasts derived from lateral equivalent embedded crusts. The sandstone complexes of the second member represent amalgamated channels with intersected cross-bedded sets. The channel pinch-out features marked upward-fining exhibited by individual channels, unimodal paleocurrent indicators, and lack of lateral accretion surfaces, suggest deposition along a mainly straight, subtidal channel complex. The record of carbonate interbeds in the upper member, exhibiting wave-ripple laminations and scouring surfaces, points to relatively high energy shallow marine intervals, probably above storm wave-base, alternating with shaly offshore-dominant substrates recording burrowing (Álvaro *et al.,* 2020a).

Ibor-Guadalupe Anticline

The N150E-trending Ibor-Guadalupe Anticline is a Variscan large-scale vertical fold that displays a general box-fold geometry (Díez Balda *et al.,* 1990; García-Hidalgo, 1985). The Lower Alcudian-Domo Extremeño Supergroup crops out on its central core, and its flanks and some disconnected exposures following the axis comprise the Ibor Group, unconformably overlain by the Armorican Quartzite. The Villarta Formation displays contrasting facies associations in the vicinity of Castañar de Ibor and Almaraz towns (Fig. 1B). In the vicinity of Castañar de Ibor, the exposures of the Villarta Formation mimic the lithology, facies and sedimentary geometries reported from the Navalpino Anticline, although all the carbonates are dominantly dolomitized and patchy replaced by magnesite. Both diagenetic processes led to the record of a macroscopic secondary porosity. However, shelly-microbial reef complexes recording several superposed replacement phases to dolomite and magnesite still display recognizable uplift-preserved *Cloudina* microfossils (Jensen *et al.,* 2019) (Fig. 5E).

In the vicinity of Almaraz, the right bank of the Tagus river (Arrocampo section sensu García-Hidalgo, 1985) offers a contrasting succession of impure dolostone/marlstone alternations. Recently, Álvaro *et al.* (2024b) subdivided the succession, 242m thick, into two sequences bounded by a breccia level. The lower sequence shows high-frequency cycles, up to 6.8m, composed of the superposition of marly claystone to dolostone strata, the latter showing, from bottom to top, a succession of scouring lenticular channels and amalgamated lenticular packages, with undulatory bedding planes and cross-stratified to low-angle sets (Fig. 5F), topped by crinkly to wavy stromatolitic beds. The uppermost cycle shows a fifth facies comprising herringbone structures (Fig. 5G). Both cross-bedded sets and herringbone structures display N–S palaeocurrents. A breccia wedge, up to 1.2m thick, separates both sequences. The breccia is polymictic, polymodal (granule to boulder) in size and poorly sorted, with disorganized and non-graded, clast-supported fabrics (Fig. 5H). The upper sequence consists of small-scale cycles, up to 8.2m thick, grading vertically, from monotonous shales and marlstones to medium-bedded, wavy to undulated, peloidal packstone-grainstone intervals forming low-angle to parallel laminated and subsidiary cross-stratified sets (Álvaro *et al.,* 2019b).

The bundles of both sequences display shallowing-upward (shoaling) cycles, ranging from offshore to peritidal environments locally punctuated by microbial crusts. The chaotic megabreccia that separates the sequences reflects a tectonic event, likely produced by a normal fault, which would have caused coeval hanging-wall subsidence and footwall uplift (Álvaro *et al.,* 2024b).

Great Central Extremenian Anticlinorium

The southeastern edge of the GCEA comprises carbonate outcrops in the vicinities of the Sierra de la Zarzuela and Orellana and Talarrubias villages (Fig. 1B). As stated above, the carbonates have received local topographic names, such as Talarrubias Dolostone and the Collado de la Liebre sandstone/shale alternations and top dolostone (Pieren Pidal, 2000). The lower Talarrubias dolostone, up to 4m thick, consists of a single dark grey massive to lenticular and bedded dolostone that, in thin-section, displays recrystallized ooids, oncoids and intraclasts arranged in decimetre-thick lenticular sets. The middle Collado de la Liebre sandstone/shale alternations show coarsening-upward and thickening cycles, up to 4m thick, locally punctuated by centimetre-thick conglomeratic lags. The uppermost Collado de la Liebre dolostone bed (Fig. 5I), up to 6m thick, consists of dark limestone interbeds encased in homogeneous green shales, rich in wavy ooidal sets interrupted by stromatolitic lenses rich in fenestral textures with birdseyes. The carbonates commonly recorded several replacing episodes to Fe-Dolomite and

ankerite, which have locally erased any original microfacies (Pieren Pidal, 2000).

The three lithostratigraphic units reflect successive shoaling-upward cycles from open-sea shaly substrates to either ooidal shoals, capped by microbial crusts, or sandy barrier sets.

Salamanca-Hurdes Dome

Unit IV of Valladares (1995) and Valladares *et al.* (2000) is dominated by monotonous to laminated black shales, rich in pyrite clusters and lacking burrowing remains, locally interrupted by a slope-related lenticular deposit, up to 260m thick and 3km wide. The latter displays amalgamated clast-supported breccia wedge sets, olistostromes and slumps crosscutting polymictic conglomeratic to calcarenitic beds with subsidiary phosphatic clasts and crusts, and sandstone/carbonate alternations. The couplets are arranged as thinning- and fining-upward cycles, up to 1.5m thick, capped by black shale interbeds.

The kerogenous shales represent low-energy clayey substrates developed under anoxic conditions, punctuated by a composite slope-related apron at the base of a fault scarp, which was interpreted by Valladares (1995) as a tectonically active half-graben, downthrown to the SW.

MAIN DIAGENETIC PROCESSES

Diagenetic processes were considered before selecting the adequate samples for further geochemical analyses. The carbonates of the Villarta Formation and lateral equivalents share similar early diagenetic processes: their carbonate cements are reported below in chronological order. The early-diagenetic indicators are crosscut by pressure dissolution features, such as solution seams and stylolites, which reflect the beginning of late diagenesis.

i) The partial or complete recrystallization of matrix to microsparite and pseudosparry mosaics (calcite phase, Cal1) is ubiquitous. Microfossils (*e.g.* from *Cloudina*-microbial reefs; Fig. 6A–B) and allochems (intraclasts, oncoids, ooids and peloids) can be easily recognized with CL. The subsequent mosaics of calcite pseudospar crystals (Cal2) show interlocking textures. Neomorphism can be related to the occlusion of intra- (shelly) and interparticle pores and, in reefal flanks, replacement of evaporitic pseudomorphs as nonluminescent to dull brown block mosaics (Álvaro *et al.,* 2020a).

ii) Some carbonates, such as the whole Arrocampo log, consist of replacive (fabric-nondestructive) microspar dolomite (dolomite phase, Dol1). Crystals are closely packed forming anhedral mosaics with irregular, intercrystalline boundaries. They finely preserve fenestral pores, stromatolitic laminae and peloidal textures suggesting a near-surface dolomitization. This dolomite is CL nonluminescent (Álvaro *et al.,* 2024b).

iii) A phase of fabric-destructive dolomitization (*e.g.* upper member at the Villarta stratotype) developed afterward. Nonferroan planar dolomite (dolomite phase, Dol2) shows either euhedral or subhedral crystal textures (Fig. 6D–E). Distinct nonzoned rhombs occur related to significant amounts (<10% in volume) of intercrystalline porosity. Dolomite Dol2 commonly shows homogeneous, moderate to dull, brownish luminescence (Álvaro *et al.,* 2020a; Herrero *et al.,* 2011).

iv) Carbonate exposures unconformably overlain by the Lower Ordovician Armorican Quartzite (reflecting the Toledanian tectonic phase; Álvaro *et al.,* 2020b; Casas *et al.,* 2024) were strongly affected by a Furongian–earliest Tremadocian episode of uplift, subaerial exposure and denudation. Carbonates exhibiting solution vugs and karstic features are common in the proximity of the unconformity (Fig. 6F). Their secondary porosities are occluded with both silty material and ferroan dolomite cements, the latter widely replacing the former diagenetic processes. Cements of ferroan dolomite (Mg/Fe ratio >4) and subsidiary ankerite (<4) appear as rhomb mosaics crosscutting the aforementioned textures (Fig. 6D). Rhombs (Dol3) typically display a distinct zonation under CL (Fig. 6C) and BSE, with massive cores, locally preserving Cal1-2 mosaics, coated by outer zones with dull-orange to nonluminescent bands. Macroscopically, the dolomitization fronts display an intense reddish aspect (Álvaro *et al.,* 2020a).

v) Late diagenetic processes are strongly preserved in areas directly affected by Variscan fissuring and cleavage. Some outcrops of the Villarta Formation in the Ibor-Navalpino Anticline (*e.g.* in the vicinity of Castañar de Ibor) show a replacement to magnesite following bedding planes, fissures and stylolites (Fig. 6G–H). Their association with talc and forsterite suggests the replacement was influenced by hydrothermal fluids (Herrero *et al.,* 2011; Fig. 7A–B).

Stable isotopes

A compilation of $\delta^{13}C$ (V-PDB) and $\delta^{18}O$ (V-SMOW) isotopic datasets from the Pastores log (Valladares *et al.,* 2006), the reefal complexes of the Villarta stratotype (Álvaro *et al.,* 2020a) and the Arrocampo section (Álvaro *et al.,* 2024b) is illustrated in Figure 7B. In Unit IV at Pastores, $\delta^{13}C$ values range between −8.7 and −0.5‰ and $\delta^{18}O$ ones between −15 to −8.8‰. Mg/Ca ratios exclude dolomitization processes, but the relative low values of Mn (61–340ppm) and Mn/Sr ratios (0.050–0.591) reflect the influence of diagenesis and burial. The bivariate $\delta^{13}C$

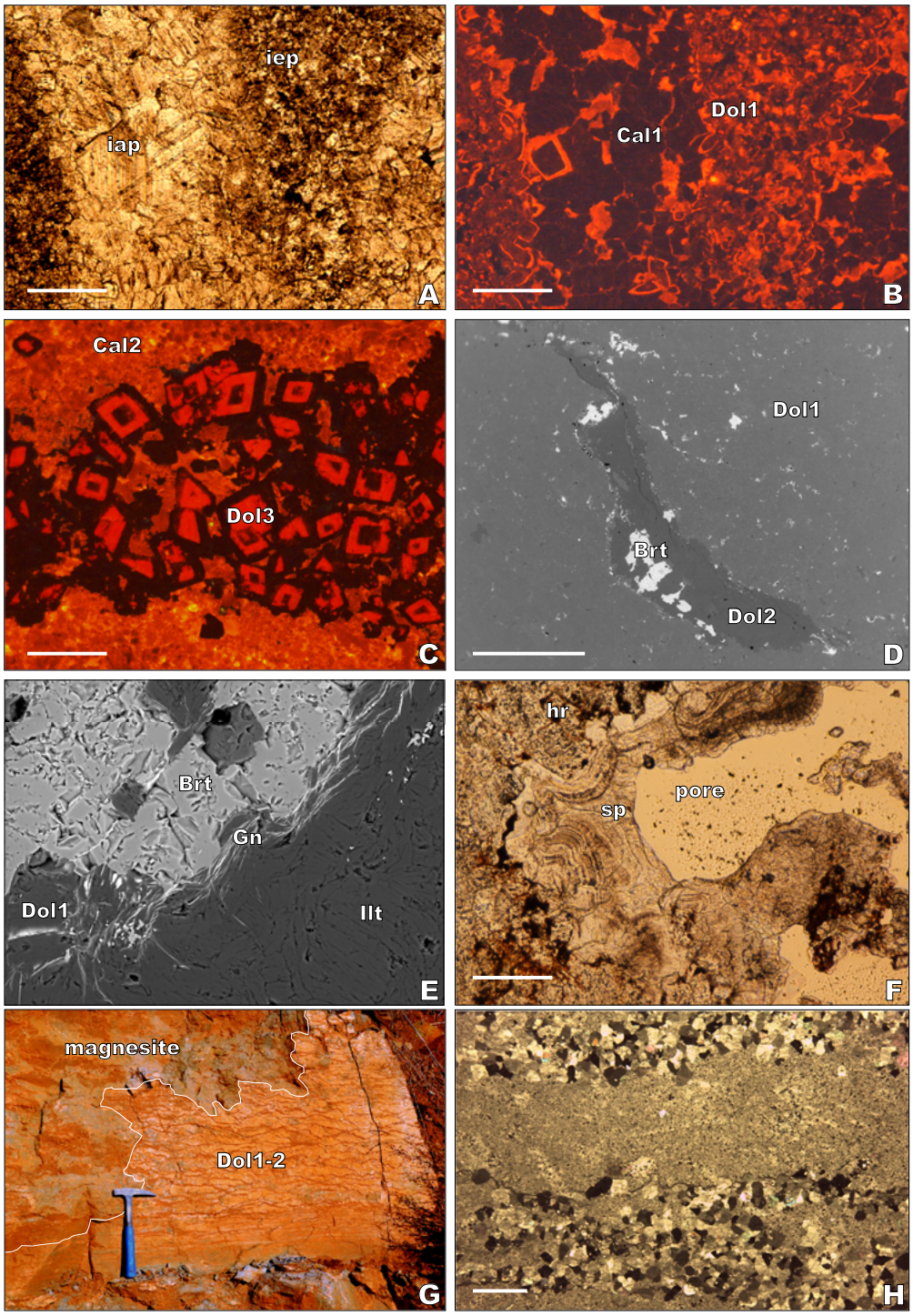

FIGURE 6. Texture of the representative diagenetic processes recorded in the Villarta Formation. A) Thin-section photomicrograph showing the pseudomorphic recrystallization recorded by the *Cloudina* walls at the stratotype and the occlusion of intraparticular and interparticular pores; parallel light; scale bar= 500μm. B) Same thin-section under cathodoluminescence showing the onset of nonluminescent (Cal1) and reddish (Dol1) crystals; scale bar= 500μm. C) Cal2 calcite cements associated with fissuring and veining associated with Fe-Dolostone (Dol3) from the upper member at the stratotype; scale bar= 500μm. D) SEM-BSE photomicrographs of a vein Dol2 clast, encasing patches of hydrothermal barite, embedded in a dolostone bed (Dol1) of the Arrocampo section; scale bar= 1mm. E) SEM-BSE photomicrographs of a hydrothermal vein crosscutting a marly dolostone bed in the Arrocampo section showing intergrowths of barite and galena; scale bar= 50μm. F) Thin-section photomicrograph showing a secondary open pore, affecting a dolomitized host rock, with the wall encrusted by a speleothem, reflecting the influence of the Toledanian tectonic phase in the upper member at the stratotype; scale bar= 500μm. G) Magnesitization front (lined) affecting a previously dolomitized (Dol1-2) bed in Castañar de Ibor. H) Thin-section photomicrograph of microsparry dolomite/magnesite (with hexagonal to subquadrate sections) alternations following plane stratification joints from Castañar de Ibor; scale bar= 2mm. Abbreviations: Brt= Barite, Cal1-2= Calcite phases, Dol1-3= Dolomite phases, Gn= Galena, hr= host rock, iap= intraparticular pore in *Cloudina* shell, iep= interparticular pore, Ilt= Illite and sp= speleothem.

vs. $\delta^{18}O$ plot yields a moderate correlation coefficient (r^2=0.531) reflecting a significant diagenetic isotopic reset (Álvaro, 2020).

The *Cloudina*-microbial reef complexes of the Villarta stratotype display different groups based on their $\delta^{13}C$ and $\delta^{18}O$ isotopic composition. The recrystalized reefal calcite cores, the marine calcite and dolomite cements, and the meteoric ferroan dolomite cement ranges from –0.03 to +2.6‰, –3 to +1.6‰, from –3.4 to –1 , and from –5.6 to –0.8‰, respectively for $\delta^{13}C$; and from –14.6 to –12‰, from –15.4 to –10.4‰, from –14.9 to –10.5, and from –8,2 to –5.2‰, respectively for $\delta^{18}O$.

Finally, samples analyzed throughout the two above-reported sequences of the Arrocampo section display $\delta^{13}C$ values ranging from –5.0 to –1.5‰, and $\delta^{18}O$ values ranging from –12.1 to –8.5‰. Mn/Sr ratios show two distinct groups: from 4.4 to 6.3 in the lower sequence, and from 0.008 to 0.003 in the upper one (Álvaro *et al.,* 2024b). Carbonates with Mn/Sr ratios <3.0 are considered to be adequate for chemostratigraphic analysis (Kaufman *et al.,* 1993), which excludes the carbon isotope data from the lower sequence for chemostratigraphic comparisons, as they reflect the progressive influence of downward infiltrating meteoric waters (Menzies *et al.,* 2014). This meteoric influence is related to the fractures connecting the megabreccia wedge that caps the erosive unconformity that tops the lower sequence.

As claimed by Álvaro (2020), recrystallization patterns to micro- and pseudosparite would be associated with a diagenetic trend toward lower $\delta^{18}O$ values. As a result, the depleted values of $\delta^{18}O$ in the Villarta carbonates would point to diagenetic and burial influence. Meteoric calcite cements (Cal1-Cal2) display $\delta^{13}C$ values similar to those of reefal cores, but comprising larger variations in $\delta^{18}O$. Primary dolomitization processes involved a distinct fall in $\delta^{13}C$ values, but still sharing the same ranges of $\delta^{18}O$ than Cal1-2. Finally, the meteoric precipitation of Fe-Dolomite (Dol3), strongly influenced by the Furongian (Toledanian) uplift and subaerial exposure reported in the area (Álvaro *et al.,* 2020b), displays lower values of $\delta^{13}C$, and $\delta^{18}O$ data shifting toward less negative values. The latter oxygen isotopic migration toward less-negative values and the lack of distinct modifications in the carbon isotope composition (from Dol1 to Dol3) may be interpreted as a result of the influence of low-temperature meteoric fluids with $\delta^{13}C$-depleted CO_2 contents, probably associated with the subaerial exposure and denudation involved under the Furongian–early Ordovician (Toledanian) uplift (Fig. 7).

Recently, Zhang *et al.* (2024) analyzed 81 whole-rock carbonate samples from the Villarta stratotype for chemostratigraphy. The authors linked the most negative values of $\delta^{18}O$ to a supposed recrystallization of original aragonite. However, Álvaro *et al.* (2020) had previously illustrated the well-preserved microbial and skeletal textures of these reefal limestones, precluding any aragonitic precursor. Seven $\delta^{13}C$ values from a single

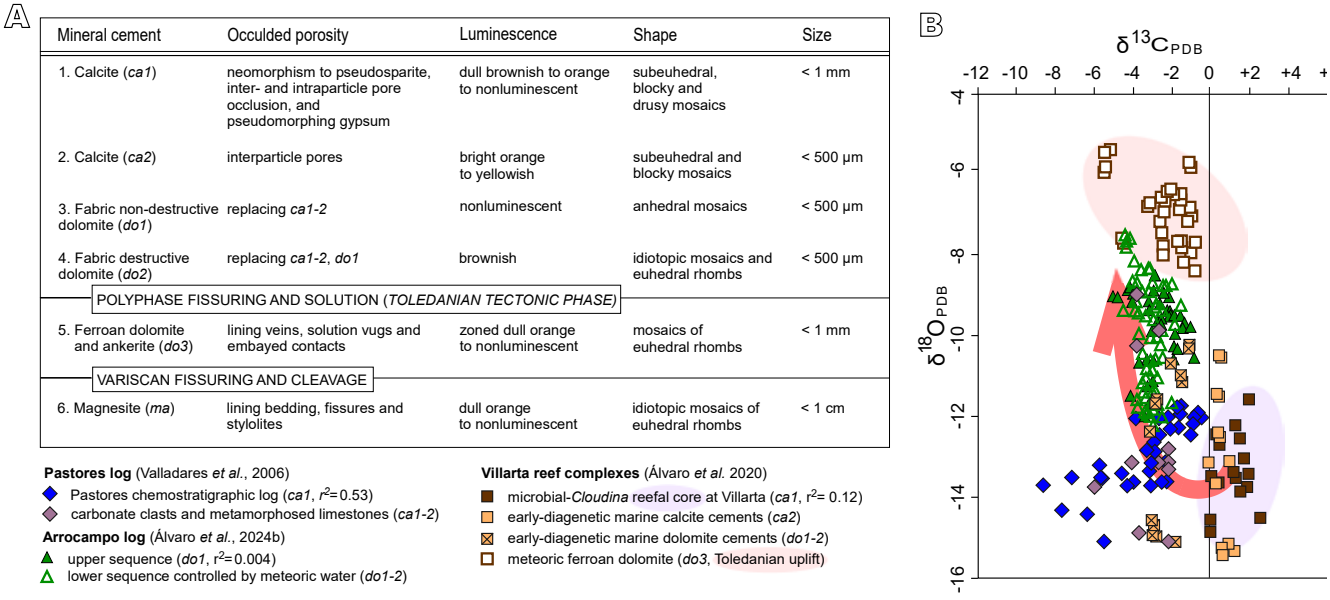

FIGURE 7. A) Idealized diagenetic and hydrothermal succession of carbonate cements recorded in the Villarta Formation throughout the Central Iberian Zone; based on Herrero *et al.* (2011) and Álvaro *et al.* (2020a, 2024b). B) Carbon and oxygen isotope cross-plot of the calcite and early-diagenetic dolomite phases reported in the text. Progressive dolomitization (arrowed) follows a clear trend in isotopic signature toward lighter δ^{13}CPDB and heavier δ^{17}OPDB values; based on Valladares *et al.* (2006) and Álvaro *et al.* (2020a, 2024b).

dolostone bed, ranging from about 0 to –9‰ VPDB, were used by the authors to locate a negative chemostratigraphic shift. Despite the lack of any chronostratigraphic control, these data were correlated with the Basal Cambrian Carbon isotope Excursion (BACE). However, such a mixture of $\delta^{13}C$ values simply reflect the mixture of early-diagenetic marine dolomite (Dol1-2) and late-diagenetic meteoric ferroan dolomite (Dol3) cements (see their $\delta^{13}C$ values in Fig. 7B). Such chemostratigraphic interpretation seems speculative and based on the lack of petrographic revision of the diagenetic cements recorded in these limestone and dolostone strata.

REE+Y DATASETS

Only the above-reported pseudosparry mosaics (Cal1) and replacive (fabric-nondestructive) microscopar dolomite (Dol1) have been targeted for REE+Y analysis. The impure (silty) carbonates interbedded in the Villarta Formation and its lateral equivalents (*i.e.* Hinojosas and Collado de la Liebre dolostone units) comprise geochemical values ranging from 17 to 53wt% CaO and 0.23 to 19.7wt% MgO, reflecting Mg/Ca ratios from 0.04 to 1.71 (calcite to dolomite). However, there are no systematic differences in the REE+Y patterns between dolomitized and non-dolomitized samples (Fig. 8A). The terrigenous content is as well very variable, ranging from 0.8 to 42wt% SiO_2, 0.2 to 9.3wt% Al_2O_3, and 0.5 to 14.7wt% Fe_2O_3 (Table I, Appendix). SiO_2, K_2O and TiO_2 exhibit a linear correlation with Al_2O_3 reflecting their association with micas, clay-rich and feldspar components in the sedimentary rocks (r^2= 0.74, 0.80 and 0.98, respectively; Fig. 8B–E). Except three samples, all the datasets show Y/Ho ratios <44 reflecting a distinct detrital influence in the REE+Y framework (Fig. 8F). The absence of correlation between Th concentrations and Y/Ho ratios suggests other processes influencing REE patterns, such as diagenetic and hydrothermal processes (Schröder and Grotzinger, 2007).

The most critical sources of contamination are continent-derived detrital material, notably clay minerals, Fe-Mn-oxydroxides and sulphides. Nothdurft *et al.* (2004) documented how shale contamination as little as 2% may alter the REE+Y pattern of marine carbonates to such an extent that elemental anomalies become effectively eliminated, resulting in flat, uniform shale-normalized patterns, which is not the case here. Useful monitors for the extent of terrestrial detrital influence are the concentrations of elements included in zircon and clay minerals, such as Zr, Th and Al. Moderate to strong positive correlation does exist between ΣREE+Y and Zr (r^2= 0.69), Th (r^2= 0.93) and Al (r^2=0.67) concentrations (Fig. 9A–C). These values decrease significantly if only those samples with low ΣREE concentrations (<25ppm) are analyzed: Zr (r^2= 0.26), Th (r^2= 0.72), Al (r^2= 0.01).

Regarding Ce anomalies, Shields and Stille (2001) proposed some parameters to track post-depositional alterations. Positive correlations in Eu/Eu* vs Ce/Ce*, (Dy/Sm)n vs Ce/Ce*, ΣREE+Y vs Ce/Ce* would follow post-depositional increases in Ce/Ce* (*i.e.* development of absent or positive Ce anomalies). However, the values yielded by the analyzed samples (r^2= 0.02, 0.03 and 0.06, respectively; Fig. 9D–F) suggest no significant diagenetic influence. The lack of correlation between Ce/Ce* and P (r^2= 0.03; Fig. 9G) also rejects any significant influence of authigenic phosphate inducing negative Ce anomalies (Pattan *et al.*, 2005).

According to the bulk REE concentrations, the analyzed samples are depleted in ΣREE relative to PAAS (Fig. 10A–B). Samples from Collado de la Liebre display the highest ΣREE values. After plotting the REE contents versus PAAS standard, two spectra are highlighted, which share similar Light REE (LREE) values slightly to moderately more fractionated than Heavy REE (HREE) ones, despite some subsidiary flat patterns, strongly marked by a common Eu anomaly in the spider-diagram. The presence or lack of positive Ce anomalies in the figures allows the distinction of two groups (Fig. 10A–B).

The light to heavy REE ratios can be evaluated by the La(SN)/Yb(SN) and Pr(SN)/Yb(SN) fractionation indexes, two assessments of the relative enrichment of HREE over LREE values, which ranges from 0.4 to 1.6 and 0.5 to 2.1, respectively. These values suggest that LREE are moderately to non-depleted by comparison with HREE. All the analysed samples display slight to moderate positive Eu anomalies (Eu/Eu*= 1.2 to 1.9; see Fig. 10C). This indicator would reflect both the contribution of plagioclase from the arc- and proximal retroarc-related sources, as well as the influence of penecontemporaneous high-temperature hydrothermal activity (Planavsky *et al.*, 2010), an influence supported by the ubiquitous record of hydrothermal dykes, which worked as sources for vein sulphide, sulphate (*e.g.* barite) and quartz vein clasts (Fig. 6D–E).

The standard of Eu anomalies (Eu/Eu*) ranges from 1.2 to 1.9, and that of Y (Y/Y*) from 0.5 to 0.8. Other ratios indicating palaeoredox conditions (McKay *et al.*, 2007) are Y/Ho (26.7 to 44.1), ΣREE/Ti (21.2 to 135; Fig. 10D), U/Th (0.4 to 3.7, oxygenated if <1.25; McKay *et al.*, 2007), and V/Sc (4 to 12, oxygenated if <9.1; Madukwe, 2016).

Cerium anomalies are significant because they reflect redox conditions in the water column and related to diagenetic processes. True Ce anomalies are suggested by plotting Ce/Ce* versus Pr/Pr* values (Bau and Dulski, 1996), where all the samples from Arrocampo and single samples from Villarta, Abenójar and Pastores plot in the field IIIa, representative of positive Ce(SN) anomalies.

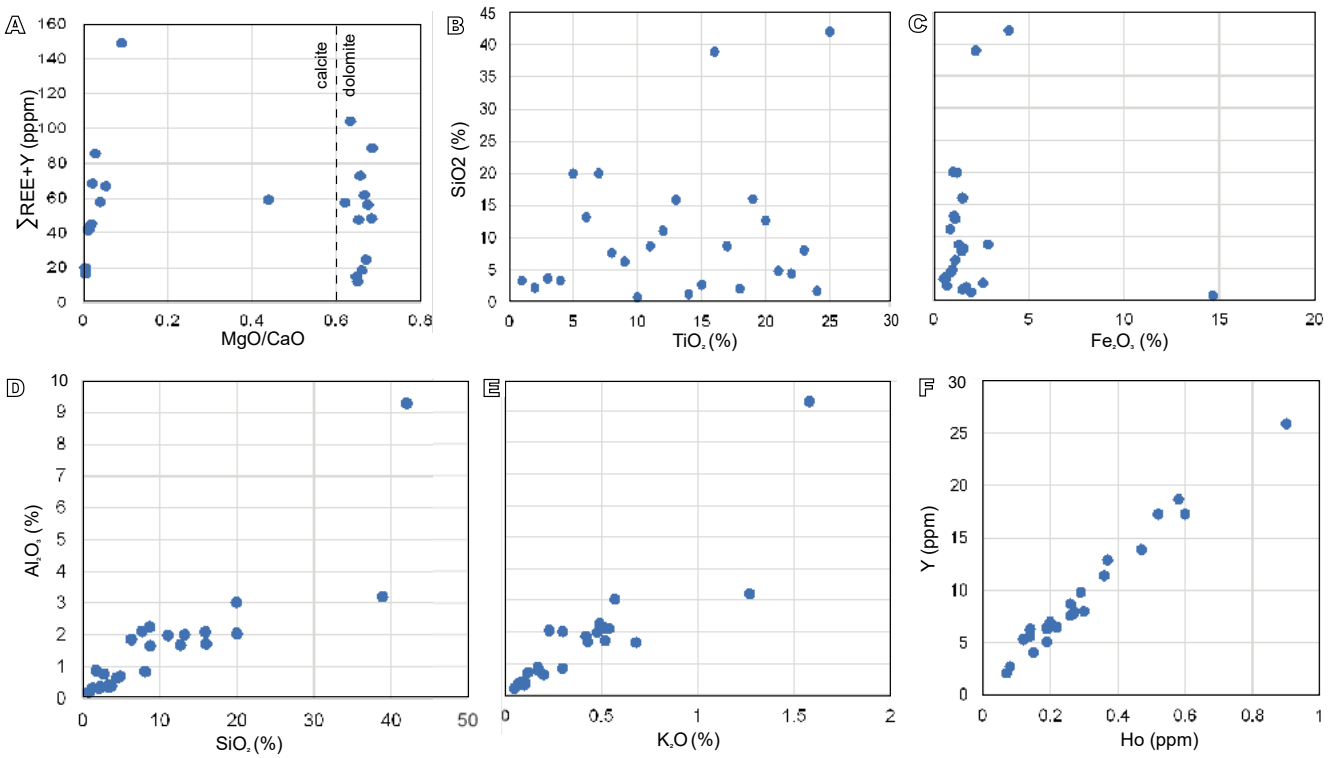

FIGURE 8. Cross-plots of oxides and REE+Y values showing the correlations described in the text. A) ΣREE+Y vs. Mg/CaO reflecting the similar composition in dolomitized and undolomitized samples. B) SiO_2 vs. TiO_2 with r^2=0.74. C) SiO_2 vs. Fe_2O_3 with r^2=0.0009, D) SiO_2 vs. Al_2O_3 with r^2=0.74. E) Al_2O_3 vs. K_2O with r^2=0.8. F) Ho vs. Y with r^2=0.97.

In summary, taking into account the contamination of REE+Y contents of the analyzed impure carbonates by terrigenous components, the geochemical dataset yielded by the Villarta Formation points to deposition of carbonates under varying redox conditions of the retroarc basin. This interpretation is supported by the distribution of kerogenous black shales in the Salamanca-Hurdes Domain. Anoxic to dysoxic waters would be associated with organic matter decomposition, despite some kind of diagenetic and/or weathering oxidation influence (Pacton *et al.,* 2011).

DISCUSSION

Retroarc foreland systems are controlled by the flexural deflection of the lithosphere led by a combination of sub- and supralithospheric loads (Catuneanu, 2004). Supracrustal loading of an orogen allows subdivision of the neighbouring foreland system into four flexural units, named wedge-top, foredeep, forebulge and backbulge depozones (DeCelles, 2012). Each renewed thrusting episode in an orogenic belt (adding load) typically results in forebulge uplift and foredeep subsidence, whereas the opposite occurs where the orogenic load is removed by extension or erosion. As a result, opposite supracrustal loading patterns can regulate the availability of accommodation space in each flexural depozone, and the erosive incision and lateral extension of major unconformities in retroarc basins (Miall, 2016; Horton, 2022).

Tentative reconstruction of the Cadomian retroarc basin

The carbonates of the Villarta Formation and the coeval Cíjara slope-related strata display wedge-shaped geometries outlining three geographical belts: a central belt of the Cíjara Formation in Spain and the Caneiro Formation in Portugal is sandwiched between two belts exhibiting episodic carbonate production (Villarta Formation in Spain and Bateiras Formation in Portugal) (Fig. 11A). The three belts share a common WNW–ESE trend which is not parallel to the Variscan-controlled Ossa-Morena/Central Iberian zonal contact.

The Iberian retroarc basin formed in front of a Cadomian arc situated to the (present-day) SW (for an interpretation of the neighbouring Ossa-Morena Zone as a mixture of Cadomian arc and proximal back-arc settings, see Bandrés *et al.,* 2002; Pereira *et al.,* 2006; Sarrionandia *et al.,* 2020). A compressive to transpressive episode is related to the so-called "Late Cadomian Folding" phase (broadly bracketed between 565 and 560Ma; Álvaro *et al.,*

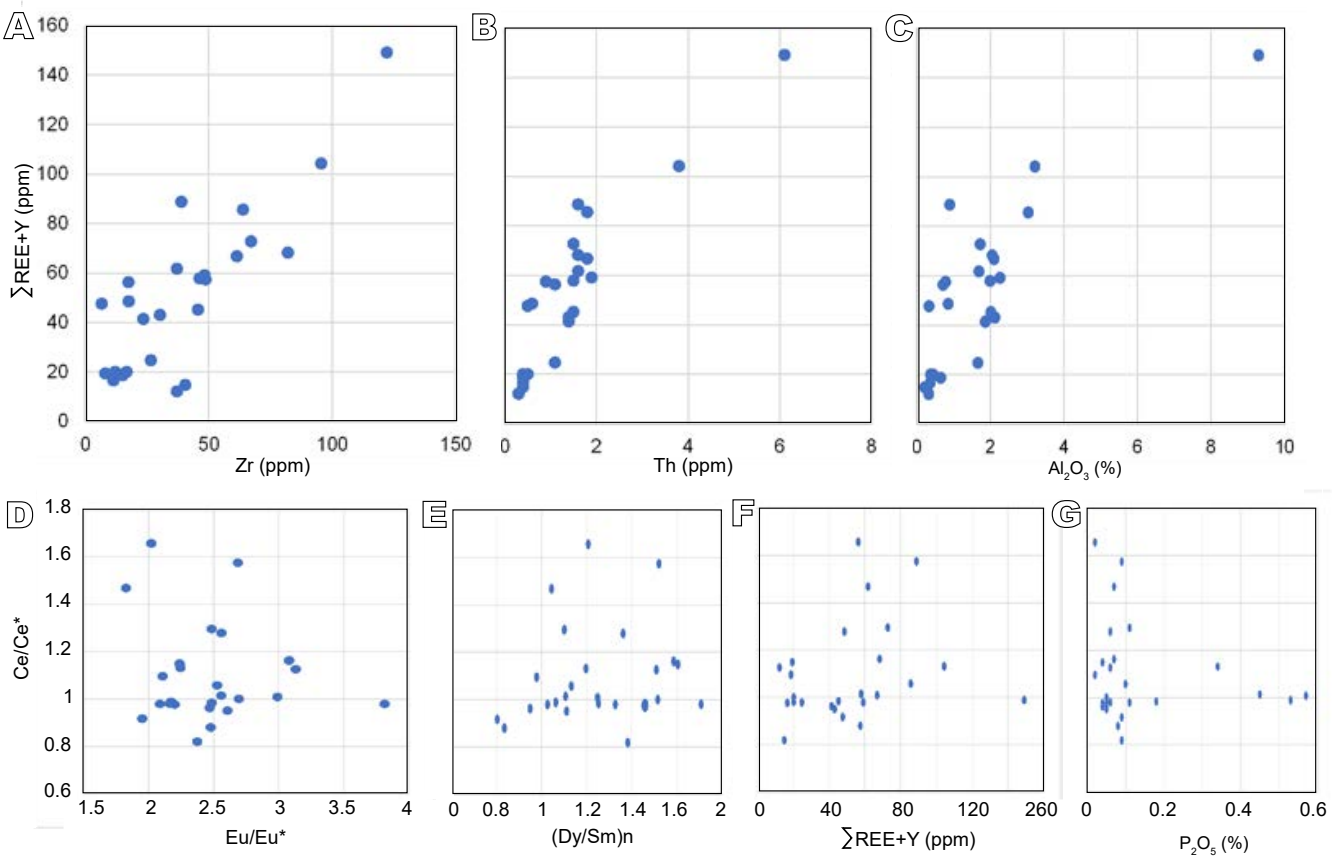

FIGURE 9. Cross-plots of the different REE+Y ratios described in the text. A) ΣREE+Y vs. Zr with r^2=0.69. B) ΣREE+Y vs. Th with r^2=0.80. C) ΣREE+Y vs. Al_2O_3 with r^2=0.67. D) Ce/Ce* vs. Eu/Eu* with r^2=0.78. E) Ce/Ce* vs. (Dy/Sm)n with r^2=0.12. F) Ce/Ce* vs. ΣREE+Y with r^2=0.96. G) Ce/Ce* vs. P_2O_5 with r^2=0.29.

2024b; Linnemann *et al.,* 2018). In the Central Iberian Zone, this episode is represented by a major unconformity marking the angular discordant to paraconformable contact separating a tilted and folded bedded palaeorelief, formed by the Lower Alcudian-Domo Extremeño Supergroup, from the overlying Ibor Group and Cíjara Formation. An uplift linked to cleavage-free folding, followed by subaerial exposure and erosive incision, has been reported in the GCEA and Alcudia Anticline (Pieren Pidal *et al.,* 1991). Their related anticlines and synclines, subsequently sealed by the Ibor and Cíjara strata, show N–S trending axial planes that, once affected by the main Variscan deformation phase, developed characteristic interference (domal) patterns (Fig. 11A).

During the following 20m.y. (ca. 560–540Ma), the orogenic strain migrated cratonward, resulting in foredeep subsidence (Central Iberian Zone) and forebulge uplift (West Asturian-Leonese and Cantabrian zones). The proximal retroarc transect, with relics preserved in the Central Iberian Zone, represents the transition between the advancing orogenic wedge and the foredeep trough (Fig. 11B). The transect recorded short-term NE-directed uplifting pulses favouring the development of the aforementioned Villarta-Cíjara-Villarta belts. The central belt developed a significant depocenter, reaching thicknesses close to 10km and infilled with prograding fan deltaic deposits punctuated by slope-related collapses (Cíjara Formation), which locally included rare carbonate clasts derived from the Villarta Formation (Álvaro *et al.,* 2019a, b).

The Cíjara belt was bounded, to the SW and NE, by uplifting blocks that episodically recorded the nucleation of carbonate factories on their tops (Villarta Formation; Álvaro *et al.,* 2019a, 2020a). Carbonate factories nucleated during episodes of tectonic quiescence and fall in siliciclastic input, both on the top of proximal uplifting platform-blocks (proximal belt; Álvaro *et al.,* 2020a), and on the edge of distal tilting blocks (cratonward distal belt; Valladares, 1995) of the foredeep through. The stepwise tectonic activity recorded in the retroarc basin led to common episodes of substrate instability generating megabreccia lobes and channels rich in unsorted debris. Palaeocurrents of the latter supplemented with those yielded by flute marks show opposite directions: N to NE polarities in the proximal and central lobes and SW ones in

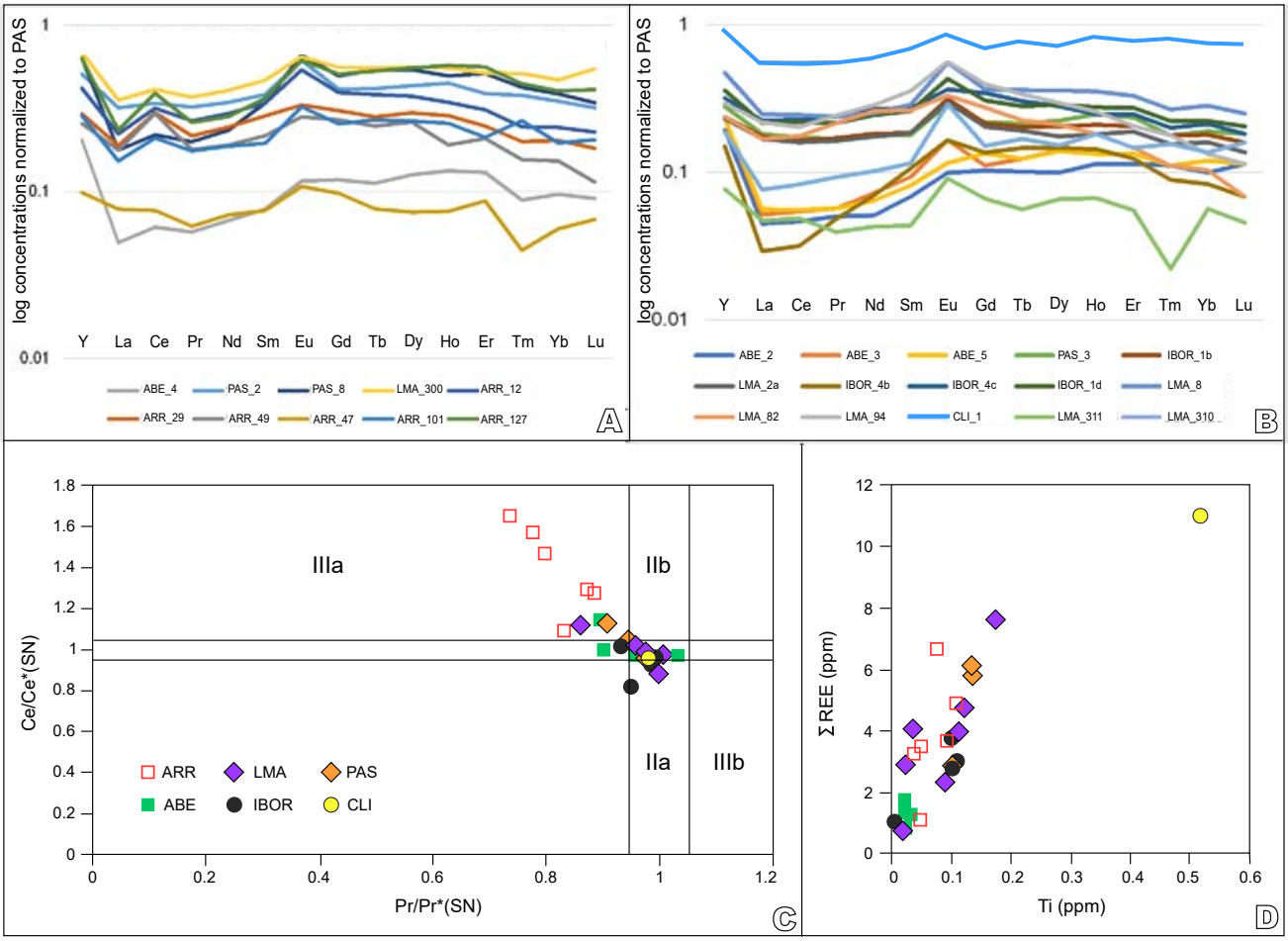

FIGURE 10. Geochemical diagrams for sampled carbonates of the Villarta Formation. A) Shale-normalized (PAAS) REE patterns exhibiting Ce and Eu anomalies. B) Similar patterns lacking Ce anomalies. C) Ce/Ce*(SN) versus Pr/Pr*(SN) diagram (Bau and Dulski, 1996); field I represents neither Ce(SN) nor La(SN) anomalies; field IIa, positive La(SN) anomalies; field IIb, negative La(SN) anomalies; field IIIa, positive Ce(SN) anomalies; and field IIIb, negative Ce(SN) anomalies; coefficient of correlation, r^2= 0.80. D) Plot of Ti vs. ΣREE showing a significant positive correlation; r^2= 0.70. Abbreviations: ABE= Abenójar log, close to the cemetery of the homonymous village, ARR= Arrocampo log (northern edge of the Ibor-Guadalupe Anticline), CLI= Collado de la Liebre log (Great Central Extremenian Anticlinorium), IBOR= Castañar de Ibor log (Ibor-Guadalupe Anticline), LMA= La Majada del Andaluz, Villarta stratotype (Navalpino Anticline) and PAS= Pastores log (Salamanca-Hurdes Dome).

the distal one (Álvaro *et al.*, 2019a, b, 2020a; Valladares, 1995), following the outlines of the foredeep trough (Fig. 11B). The most important episodes of anoxia, linked to the deposition of kerogenous black shales, are restricted to the Salamanca-Hurdes Dome and the lateral equivalent Bateiras Formation in Portugal. In contrast to the slope-related strata of the Cíjara Formation, recording REE+Y datasets pointing to persistent oxic conditions (Álvaro *et al.*, 2024a), the carbonates of the Villarta Formation recorded varying redox (oxic-dysoxic) conditions in the water column. Although the original orientation of the Cadomian retroarc foreland basin is unknown, due to the superposition of the Ordovician Toledanian tectono-magmatic phase and the Variscan deformations, it was suitable to receive oceanic upwelling linked to eutrophic episodes, as the probable cause for the episodic phosphoritic deposits recorded in the retroarc basin (Álvaro *et al.*, 2016).

Correlation of Cadomian tectonic pulses

As stated above, the so-called "late Cadomian (cleavage-free) folding event" took place between 565 and 560Ma (Álvaro *et al.*, 2024b; Linnemann *et al.*, 2018). The event is related to uplift, subaerial exposure and denudation in a proximal retroarc transect preserved in the Central Iberian Zone, whereas a relatively continuous sedimentation was recorded throughout distal (cratonward) transects of the retroarc basin (Cantabrian Zone). The return to sedimentation in the Central Iberian Zone (559–557Ma interval) is marked in the Cantabrian Zone by distinct tectonomagmatic episodes, represented by the Cudillero ignimbritic rhyolite (557±3Ma; Rubio-Ordóñez *et al.*, 2015) and the Tineo volcaniclastic sandstone (559±1Ma; Gutiérrez-Alonso *et al.*, 2004; Rubio-Ordóñez *et al.*, 2015). Subsequently, the distal retroarc transect (West Asturian-

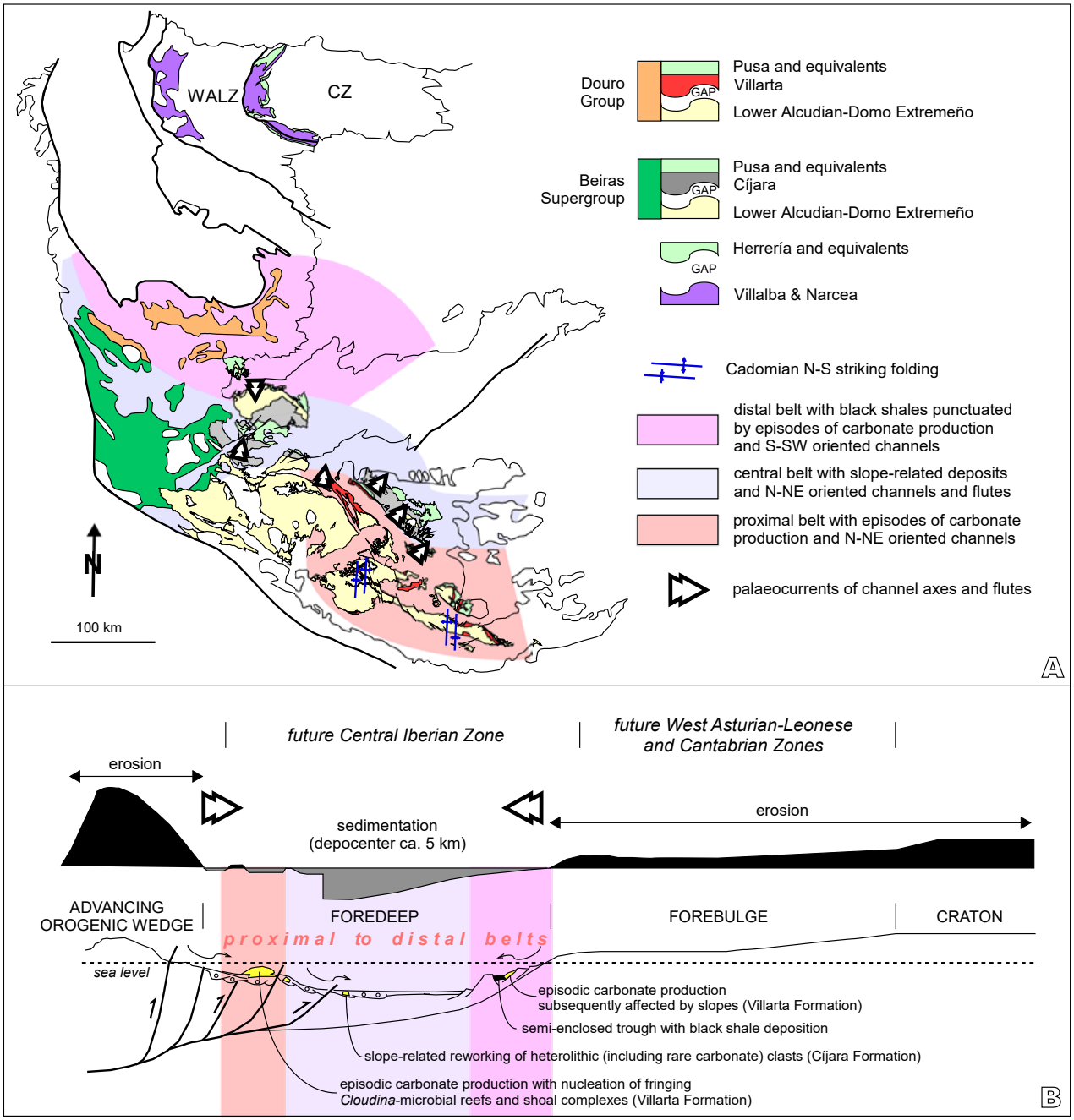

FIGURE 11. A) Sketch showing present-day geographic distribution of the upper Ediacaran to Fortunian (Terreneuvian) facies belts throughout the (Variscan) Central Iberian, West Asturian-Leonese Zone (WALZ) and Cantabrian Zone (CZ) of the Iberian Massif. B) Tentative palaeogeographic cross-section of the Cadomian retroarc foreland basin preserved in the same Variscan tectonostratigraphic zones with setting of the main carbonate factories reported in the text.

Leonese and Cantabrian zones) was definitively uplifted, exposed to subaerial exposure and denudation, becoming a forebulge. From about 560 to 550Ma, accommodation space was available in the foredeep basin (Cíjara Formation and Ibor Group), whereas the forebulge sector was uplifted and eroded. The uplifting episodes recorded by the Villarta and Cíjara formations were reflected in the forebulge by folds with E–W (present day) axes, vertical axial planes, and steep limbs resulting in a high angle unconformity with the base of the sealing Cándana and Herrería strata (Pérez-Estaún and Martínez, 1978; Gutiérrez-Alonso, 1996, 1997).

The Cadomian collapse and record of the pre-rift unconformity is diachronous throughout the arc to retroarc

transects preserved in the Iberian massif, ranging from an intra-Fortunian age in the Central Iberian Zone (Álvaro *et al.,* 2019a; Álvaro and Lorenzo, 2022) to the Cambrian Age/Stage 2 boundary interval in the Cantabrian Zone. The time span involved in the Mora/Herrería contact is not well constrained, but a maximum of ca. 20m.y. should be involved due to the lack of the lower part of the acritarch-based *Granomarginata–Leiosphaeridia* Zone (Álvaro *et al.,* 2024b; Palacios and Vidal, 1992).

CONCLUSIONS

The Central Iberian Zone of the Iberian massif preserves the nucleation, growth and demise of late Ediacaran episodes of carbonate production in a retroarc basin. They are sandwiched between two unconformities: the lower is interpreted as a Late Cadomian Folding Event (565 to 560Ma) and the upper as the Cadomian orogenic collapse, intra-Fortunian in age. The carbonate productivity recorded in the Villarta Formation (Ibor Group) developed on a mosaic of uplifted and tilted fault-bounded basement highs, both in the proximal and distal parts of the associated foredeep trough. The geometry of the sedimentary bodies and their environments point to fringing reefal and shoal and back-barrier complexes on fault-bounded highs, which commonly fed slope-related megabreccia lobes and channels controlled by sediment gravity flows and mass wasting pulses controlling the size of carbonate platform-blocks. REE+Y datasets from the impure limestones and early-diagenetic dolostones point to oxic–dysoxic conditions in the water column. In contrast, the distal part of the foredeep trough recorded kerogenous black shales and graphitic slates. The orientation of the retroarc basin somewhat allowed the influence of oceanic upwelling, which would explain the relative frequency of phosphoritic crusts.

ACKNOWLEDGMENTS

The authors appreciate the constructive revision made by Lluís Cabrera and Josep Maria Casas (UB, Barcelona). JJA warmly thanks technical support by Idoia Rosales (IGME, Tres Cantos) for carrying out CL images, and Laura Tormo (MNCN, Madrid) for SEM-BSE analysis. This work is a contribution to Spanish project PID2021-125585NB-I00 from Ministerio de Ciencia e Innovación.

REFERENCES

Álvaro, J.J., 2020. Calibrating $\delta^{13}C$ and $\delta 18O$ chemostratigraphic correlations across Cambrian strata of SW Europe and Morocco, West Gondwana. In: Montenari, M. (ed.). Carbon Isotope Stratigraphy. Stratigraphy & Time Scales, 5, 269-317.

Álvaro, J.J., Lorenzo, S., 2022. Cadomian orogenic collapse in the Ibor and Alcudia anticlines of the Central Iberian Zone, Spain. Geological Magazine, 159, 1251-1261.

Álvaro, J.J., Shields, G.A., Ahlberg, P., Jensen, S., Palacios, T., 2016. Ediacaran–Cambrian phosphorites from the western margins of Gondwana and Baltica. Sedimentology, 63, 350-377.

Álvaro, J.J., Cortijo, I., Jensen, S., Lorenzo, S., Palacios, T., Pieren, A., 2019a. Updated stratigraphic framework and biota of the Ediacaran and Terreneuvian in the Alcudia-Toledo Mountains of the Central Iberian Zone, Spain. Estudios Geológicos, 75(2), e093.

Álvaro, J.J., Jensen, S., Palacios, T., 2019b. Post-conference fieldtrip, October 21–24, 2019. Ediacaran and Terreneuvian strata surrounding the Villuercas-Ibores-Jara Geopark. Estudios Geológicos, 75(2), e121.

Álvaro, J.J., Cortijo, I., Jensen, S., Martí Mus, M., Palacios, T., 2020a. *Cloudina*-microbial reef resilience to substrate instability in a Cadomian retro-arc basin of the Iberian Peninsula. Precambrian Research, 336, 105479.

Álvaro, J.J., Sánchez-García, T., Puddu, C., Casas, J.M., Díez-Montes, A., Liesa, M., Oggiano, G., 2020b. Comparative geochemical study on Furongian–earliest Ordovician (Toledanian) and Ordovician (Sardic) felsic magmatic events in south-western Europe: underplating of hot mafic magmas linked to the opening of the Rheic Ocean. Solid Earth, 11, 2377-2409.

Álvaro, J.J., Ortiz, J.E., Neto de Carvalho, C., López-Illa, I., Sánchez-Palencia, Y., Torres, T., 2024a. Biogenicity of amorphous organic matter and bacteriomorph acritarchs preserved in wrinkle structures from the Ediacaran Cíjara Formation, Spain. The Depositional Record, 10, 51-69.

Álvaro, J.J., Jensen, S., Valverde-Vaquero, P., 2024b. Multidisciplinary re-assessment of the Ediacaran–Cambrian boundary interval in south-western Europe. Newsletters on Stratigraphy, 57, 323-357.

Álvaro, J.J., Lorenzo, S., Devaere, L., Warren, L.V., 2024c. Terreneuvian skeletonized microfossils from the Central Iberian Zone (Spain) and correlation of the Fortunian Stage throughout SW Europe. Palaeoworld, 33, 1179-1194.

Bandrés, A., Eguíluz, L., Gil Ibarguchi, J.I., Palacios, T., 2002. Geo-dynamic evolution of a Cadomian arc region: the northern Ossa-Morena Zone, Iberian Massif. Tectonophysics, 352, 105-120.

Bau, M., Dulski, P., 1996. Distribution of yttrium and rare-earth elements in the Penge and Kuruman Iron-Formations, Transvaal Supergroup, South Africa. Precambrian Research, 79, 35-55.

Byrne, R., Scholkovitz, E., 1996. Marine chemistry and geochemistry of the lanthanides. In: Gschneider, K.A., Eyring, L. (eds.). Handbook on the Physics and Chemistry of the Rare Earths. Amsterdam, Elsevier, 23, 497-593.

Calvet, F., Salas, R., 1988. Tipos de plataformas carbonatadas del Precámbrico terminal de la zona Centro-Ibérica. II Congreso de Geología de España, Granada, Comunicaciones, 1, 59-62.

Carrington da Costa, J., 1950. Noticia sobre uma carta geológica do Buçaco, de Nery Delgado. Direção Geral de Minas e Serviços Geológicos de Portugal, 28pp.

Casas, J.M., Murphy, J.B., Díez Montes, A., Sánchez-García, T., de Poulpiquet, J., Álvaro, J.J., Guimerà, J., 2024. Does the Ollo de Sapo magmatic event support Furongian–Tremadocian mantle plume activity fringing NW Gondwana? International Geology Review, 66, 1956-1970.

Catuneanu, O., 2004. Retroarc foreland systems–evolution through time. Journal of African Earth Sciences, 38, 225-242.

Clavera-Gispert, R., Carmona Bardella, A., Gratacós Torrà, O., Tolosana-Delgado, R., 2012. Incorporating nutrients as a limiting factor in carbonate modelling. Palaeogeography, Palaeoclimatology, Palaeoecology, 329-330, 150-157.

Coletti, G., El Kateb, A., Basso, D., Cavallo, A., Spezzaferri, S., 2017. Nutrient influence on fossil carbonate factories: evidence from SEDEX extractions on Burdigalian limestones (Miocene, NW Italy and S France). Palaeogeography, Palaeoclimatology, Palaeoecology, 475, 80-92.

Cortijo, I., Martí Mus, M., Jensen, S., Palacios, T., 2010. A new species of *Cloudina* from the terminal Ediacaran of Spain. Precambrian Research, 176, 1-10.

Cortijo, I., Martí Mus, M., Jensen, S., Palacios, T., 2015. Late Ediacaran skeletal body fossil assemblage from the Navalpino anticline, central Spain. Precambrian Research, 267, 186-195.

DeCelles, P.G., 2012. Foreland basin systems revisited: variations in response to tectonic settings. In: Busby, C., Azor Pérez, A. (eds.). Tectonics of Sedimentary Basins: Recent Advances. Oxford, Blackwell, 405-426.

Díez Balda, M.A., Vegas, R., González Lodeiro, F., 1990. Part IV. Central Iberian Zone. Structures. In: Dallmeyer, R.D., Martínez García, E. (eds.). Pre–Mesozoic Geology of Iberia. Berlin, Springer-Verlag, 172-188.

Dorobek, S.L., 2007. Carbonate-platform facies in volcanic-arc settings: characteristics and controls on deposition and stratigraphic development. In: Draut, A., Clift, P.D., Scholl, S.W. (eds.). Formation and Application of the Sedimentary Record in Arc Collision Zones. Geological Society of America, 436 (Special Paper), 55-90.

García-Hidalgo, J.F., 1985. Estratigrafía y sedimentología del Alcudiense superior en los anticlinorios de Ibor y Navezuelas-Robledollano. Seminarios de Estratigrafía (Serie Monografías), 12, 1-190.651

Gutiérrez-Alonso, G., 1996. Strain partitioning in the footwall of the Somiedo Nappe: structural evolution of the Narcea Tectonic Window, NW Spain. Journal of Structural Geology, 18, 1217-1229.

Gutiérrez-Alonso, G., 1997. La estructura del Antiforme del Narcea y su relación con los Mantos occidentales de la Zona Cantábrica. Parte II: el sector oriental. Stvdia Geologica Salmanticensis, 33, 121-175.

Gutiérrez-Alonso, G., Fernández-Suárez, J., Weil, A.B., 2004. Orocline triggered lithospheric delamination. In: Sussman, A.J., Weil, A.B. (eds.). Orogenic Curvature: Integrating Paleomagnetic and Structural Analyses. Geological Society of America, 383 (Special Paper), 121-131.

Halfar, H., Godinez-Orta, L., Mutti, M., Valdez-Holguin, B., 2004. Nutrients and temperature controls on modern carbonate production: an example from the Gulf of California, Mexico. Geology, 32, 213-221.

Herrero, M.J., Martín-Pérez, A., Alonso-Zarza, A.M., Gil-Peña, I., Meléndez, A., Martín-García, R., 2011. Petrography and geochemistry of the magnesites and dolostones of the Ediacaran Ibor Group (635 to 542Ma), Western Spain: evidences of their hydrothermal origin. Sedimentary Geology, 240, 71-84.

Horton, B.K., 2022. Unconformity development in retroarc foreland basins: implications for the geodynamics of Andean-type margins. Journal of the Geological Society, 179, jgs2020-263.

Hufnagel, H., 2008. Kohlige Makroreste aus dem Oberen Proterozoikum der Ibor Antiklinale (Prov. Cáceres, Spanien). In: Arcega Conesa, C., Lahoz Gimeno, J. (eds.). La Vida en el Terciario: del impacto del meteorito al origen del hombre. Zaragoza, X Jornadas Aragonesas de Paleontología. Institución Fernando el Católico, 227-260.

Jensen, S., Palacios, T., 2016. The Ediacaran–Cambrian trace fossil record in the Central Iberian Zone, Iberian peninsula. Comunicaçoes Geológicas, 103, 83-92.

Jensen, S., Álvaro, J.J., Palacios, T., 2019. Pre-conference fieldtrip, October 17–18, 2019: Ediacaran, Lower Palaeozoic and landscapes within the Villuercas-Ibores-Jara UNESCO Global Geopark. Estudios Geológicos, 75(2), e120.

Kaufman, A.J., Jacobsen, S.B., Knoll, A.H., 1993. The Vendian record of Sr- and C-isotopic variations in seawater: implications for tectonics and paleoclimate. Earth and Planetary Science Letters, 120, 409-430.

Linnemann, U., Pieren, A., Hofmann, M., Drost, K., Quesada, C., Axel, G., Marko, L., Gärtner, A., Zieger, J., Jens, U., 2018. A ~565Ma old glaciation in the Ediacaran of peri-Gondwanan West Africa. International Journal of Earth Sciences, 107, 885-911.

Liu, K., Feng, Q., Shen, J., Khan, M., Planavsky, N.J., 2018. Increased productivity as a primary driver of marine anoxia in the Lower Cambrian. Palaeogeography, Palaeoclimatology, Palaeoecology, 491, 1-9.

López Díaz, F., 1995. Late Precambrian series and structures in the Navalpino Variscan Anticline (Central Iberian Peninsula). Geologische Rundschau, 84, 151-163.

Lorenzo Álvarez, S., Solé, J., 1988. La discordancia intra–precámbrica y la estratigrafía del Precámbrico superior en el sector suroriental del Anticlinal de Abenójar-Tirteafuera. Granada, II Congreso Geológico de España, Comunicaciones, 1, 115-118.

Lotze, F., 1945. Zur Gliederung der Varisziden der Iberischen Meseta. Geotektonische Forschung, 16, 78-92.

Madukwe, H.Y., 2016. Granulometric analysis of sandstone facies of the Ise Formation, Southwestern Nigeria. Journal of Multidisciplinary Engineering Science and Technology, 3, 3909-3919.

McKay, J.L., Pedersen, T.F., Mucci, A., 2007. Sedimentary redox conditions in continental margin sediments (NE Pacific)-

influence on the accumulation of redox-sensitive trace metals. Chemical Geology, 238, 180-196.

Medina, J., Rodríguez Alonso, M.D., Alonso Gavilán, G., 1998. Sedimentação em plataforma siliciclástica do Grupo das Beiras (CXG) na região de Caramulo-Buçaco (Portugal Central). Comunicaçaos do Instituto Geológico e Mineiro, 85, 39-71.

Meireles, C., Sequeira, A.J.D., Castro, P., Ferreira, N.I., 2013. New data on the lithostratigraphy of Beiras Group (Schist Greywacke Complex) in the region of Góis-Arganil-Pampilhosa da Serra (Central Portugal). Cuadernos do Laboratorio Xeolóxico de Laxe, 37, 105-124.

Menzies, C.D., Teagke, D.A.H., Craw, D., Cox, S.C., Boyce, A.J., Barrie, C.D., Roberts, S., 2014. Incursion of meteoric waters into the ductile regime in an active orogen. Earth and Planetary Science Letters, 399, 1-13.

Miall, A.D., 2016. The valuation of unconformities. Earth-Science Reviews, 163, 22-71.

Nothdurft, L.D., Webb, G.E., Kamber, B.S., 2004. Rare earth element geochemistry of Late Devonian reefal carbonates, Canning Basin, Western Australia: confirmation of a seawater REE proxy in ancient limestones. Geochimica et Cosmochimica Acta, 68, 263-283.

Pacton, M., Gorin, G.E., Vasconcelos, C., 2011. Amorphous organic matter – Experimental data on formation and the role of microbes. Review of Palaeobotany and Palynology, 166, 253-267.

Palacios Medrano, T., 1989. Microfósiles de pared orgánica del Proterozoico superior (región central de la Península Ibérica). Memorias del Museo Paleontológico de la Universidad de Zaragoza, 3, 1-91.

Palacios, T., Vidal, G., 1992. Lower Cambrian acritarchs from northern Spain: the Precambrian–Cambrian boundary and biostratigraphic implications. Geological Magazine, 129, 421-436.

Palacios, T., Eguíluz, L., Apalategui, O., Jensen, S., López Torres, L., Carracedo, M., Gil Ibarguchi, J.I., Sarrioiandía, F., Martí Mus, M., 2010. Mapa Geológico de Extremadura a escala 1:250.000. Consejería de Industria, Energía y Medio Ambiente, Junta de Extremadura, Mérida, Memoria, 222pp.

Pattan, J.N., Pearce, N.J.G., Mislankar, P.G., 2005. Constraints in using Cerium-anomaly of bulk sediments as an indicator of paleo bottom water redox environment: a case study from the Central Indian Ocean Basin. Chemical Geology, 221, 260-278.

Peláez, J.R., García-Hidalgo, J.F., Moreno-Eiris, E., Herranz Araújo, P., 1988. El nivel con carbonatos del "Alcudiense Superior" en el área de Cabezarrubias-Hinojosas (Valle del Alcudia, Ciudad Real). Geogaceta, 4, 27-28.

Pereira, M.F., Chichorro, M., Linnemann, U., Eguiluz, L., Silva, J.B., 2006. Inherited arc signature in Ediacaran and Early Cambrian basins of the Ossa-Morena Zone (Iberian Massif, Portugal): paleogeographic link with European and North African Cadomian correlatives. Precambrian Research, 144, 297-315.

Pérez-Estáun, A., Martínez, F.J., 1978. El Precámbrico del antiforme del Narcea en el sector de Tineo-Cangas de Narcea (NW de España). Trabajos de Geología, Universidad de Oviedo, 10, 367-377.

Pieren Pidal, A.P., 2000. Las sucesiones anteordovícicas de la región oriental de la provincia de Badajoz y área contigua de Ciudad Real. PhD Thesis. Madrid, Universidad Complutense, 410pp.

Pieren Pidal, A.P., 2009. Rasgos geológicos de la comarca de Puertollano y del valle del Alcudia (Ciudad Real, España). Memorias de la Real Sociedad Española de Historia Natural (2ª serie), 6, 95-132.

Pieren Pidal, A.P., Herranz Araújo, P., García Gil, S., 1991. Evolución de los depósitos continentales del Proterozoico Superior en "La Serena", Badajoz (Zona Centro lbérica). Cuadernos do Laboratorio Xeolóxico de Laxe, 16, 179-191.

Planavsky, N., Bekker, A., Rouxel, O.J., Kamber, B., Hofmann, A., Knudsen, A., Lyons, T.W., 2010. Rare earth element and yttrium compositions in Archean and Paleoproterozoic Fe formations revisited: new perspectives on the significance and mechanisms of deposition. Geochimica et Cosmochimica Acta, 74, 6387-6405.

Pourmand, A., Dauphas, N., Ireland, T.J., 2012. A novel extraction chromatography and MC-ICP-MS technique for rapid analysis of REE, Sc and Y: revising CI-chondrite and Post-Archean Australian Shale (PAAS) abundances. Chemical Geology, 291, 38-54.

Rodríguez Alonso, M.D., 1984. El complejo esquisto-grauváquico en el área de Las Hurdes y Sierra de Gata, provincias de Salamanca y Cáceres, España. Cuadernos de Geología Ibérica, 9, 37-80.

Rodríguez Alonso, M.D., Peinado, M., López-Plaza, M., Franco, P., Carnicero, A., Gonzalo, J.C., 2004. Neoproterozoic–Cambrian synsedimentary magmatism in the Central Iberian Zone (Spain): geology, petrology and geodynamic significance. International Journal of Earth Sciences, 93, 897-920.

Rubio-Ordóñez, A., Gutiérrez-Alonso, G., Valverde-Vaquero, P., Cuesta, A., Gallastegui, G., Gerdes, A., Cárdenes, A., 2015. Arc-related Ediacaran magmatism along the northern margin of Gondwana: geochronology and isotopic geochemistry from northern Iberia. Gondwana Research, 27, 216-227.

San José, M.A. de, 1984. Los materiales anteordovícicos del anticlinal de Navalpino. Cuadernos de Geología Ibérica, 9, 81-117.

San José, M.A. de, Rábano, I., Herranz, P., Gutiérrez Marco, J.C., 1992. El Paleozoico inferior de la zona Centro Ibérica meridional. In: Gutiérrez-Marco, J.C., Saavedra, J., Rábano, I. (eds.). Paleozoico Inferior de Ibero-América. Mérida, Extremadura University Press, 503-521.

Sarrionandia, F., Ábalos, B., Errandonea-Martin, J., Eguíluz, L., Santos-Zalduegui, J.F., García de Madinabeitia, S., Carrecedo-Sánchez, M., Gil Ibarguchi, J.I., 2020. Ediacaran–Earliest Cambrian arc tholeiite and adakite associations of the Malcocinado Formation (Ossa-Morena Zone, SW Spain): juvenile continental crust and deep crustal reworking in northern Gondwana. Lithos, 372-373, 105683.

Schröder, S., Grotzinger, J.P., 2007. Evidence for anoxia at the Ediacaran–Cambrian boundary: the record of redox-sensitive trace elements and rare earth elements in Oman. London, Journal of the Geological Society, 164, 175-187.

Sequeira, A.J.D., 2011. Microfossils of Beiras Group (Monfortinho – Salvaterra do extremo, Beira Baixa, Central Portugal). Comunicações Geologicas, 98, 55-60.

Shields, G., Stille, P., 2001. Diagenetic constraints on the use of cerium anomalies as palaeoseawater redox proxies: an isotopic and REE study of Cambrian phosphorites. Chemical Geology, 175, 29-48.

Simón, J., 2018. A transitional Ediacaran–Cambrian biota in the Abenójar anticline (Iberian Massif, Spain). Estudios Geológicos, 74(2), e084.

Talavera, C., Martínez Poyatos, D., González Lodeiro, F., 2015. SHRIMP U–Pb geochronological constraints on the timing of the intra–Alcudian (Cadomian) angular unconformity in the Central Iberian Zone (Iberian massif, Spain). International Journal of Earth Sciences, 104, 1739-1757.

Ugidos, J.M., Barba, P., Valladares, M.I., 2020. Review of the Upper Ediacaran–Lower Cambrian detrital series in Central and North Iberia: NE Africa as possible source area. In: Montenari, M. (ed.). Carbon Isotope Stratigraphy. Stratigraphy & Time scales, 5, 147-268.

Valladares, M.I., 1995. Siliciclastic-carbonate slope apron in an immature tensional margin (Upper Precambrian–Lower Cambrian), central Iberian Zone, Salamanca, Spain. Sedimentary Geology, 94, 165-186.

Valladares, M.I., Barba, P., Ugidos, J.M., Colmenero, J.R., Armenteros, I., 2000. Upper Neoproterozoic–Lower Cambrian sedimentary successions in the Central Iberian Zone (Spain): sequence stratigraphy, petrology and chemostratigraphy. Implications for other European zones. International Journal of Earth Sciences, 89, 2-20.

Valladares, M.I., Ugidos, J.M., Barba, P., Fallick, A.E., Ellam, R.M., 2006. Oxygen, carbon and strontium isotope records of Ediacaran carbonates in Central Iberia (Spain). Precambrian Research, 147, 354-365.

Vidal, G., Palacios, T., Gámez-Vintaned, J.A., Díaz Balda, M.A., Grant, S.W.F., 1994. Neoproterozoic–early Cambrian geology and palaeontology of Iberia. Geological Magazine, 131, 729-765.

Zhang, K., Shields, G.A., Zhou, Y., Strauss, H., Struck, U., 2024. The basal Cambrian carbon isotope excursion revealed in the Central Iberian Zone, Spain. Precambrian Research, 411, 107526 .

Manuscript received February 2024;
revision accepted June 2024;
published Online September 2024.

APPENDIX I

TABLE I. Whole-rock geochemical dataset of the Ediacaran impure carbonate samples from the Villarta Formation (=Hinojosa and Talarrubias/Collado de la Liebre units), Central Iberian Zone

	SiO_2	Al_2O_3	Fe_2O_3	MgO	CaO	Na_2O	K_2O	TiO_2	P_2O_5	MnO	Cr_2O_3	Ba	Ni	Sc	LOI
samples	%	%	%	%	%	%	%	%	%	%	%	ppm	ppm	ppm	
ABE 9_2	3.4	0.36	0.53	0.31	52.13	0.02	0.07	0.02	0.04	<0.01	<0.002	92	28	<1	12.8
ABE9_3	2.31	0.37	0.7	0.25	53.05	0.02	0.07	0.02	0.05	0.01	<0.002	112	31	<1	13
ABE9_4	3.72	0.4	0.62	0.28	52.53	<0.01	0.08	0.02	0.04	<0.01	<0.002	157	24	<1	12
ABE9_5	3.41	0.44	0.64	0.23	52.42	<0.01	0.1	0.03	0.06	0.01	<0.002	381	30	<1	12.4
PAS_2	19.95	3.03	1.23	1.14	39.5	0.52	0.57	0.13	0.1	0.03	0.003	444	31	3	13.6
PAS_3	13.23	2.01	1.08	0.88	44.45	0.47	0.3	0.1	0.18	0.02	0.003	238	33	2	17.1
PAS_8	20.03	2.05	1.01	0.9	40.64	0.61	0.23	0.13	0.07	0.06	0.003	103	32	2	14
IBOR_1b	7.69	2.12	1.47	0.68	47.54	0.05	0.52	0.11	0.05	0.02	0.003	101	35	3	11.6
IBOR_1d	6.31	1.86	1.14	0.59	48.76	0.06	0.42	0.1	0.04	0.02	0.003	90	27	2	12.5
IBOR_4b	0.8	0.21	14.67	14.25	21.99	<0.01	0.05	<0.01	0.09	0.39	<0.002	7	30	<1	17
IBOR_4c	8.74	2.26	2.85	12.88	29.31	0.05	0.49	0.1	0.11	0.11	0.002	84	34	3	12.7
LMA-2A	11.1	1.99	0.87	1.82	44.85	0.4	0.48	0.11	0.45	0.04	0.003	49	34	2	17.8
LMA_8	15.93	2.1	1.53	2.21	41.21	0.36	0.54	0.12	0.57	0.06	0.003	51	36	2	15.2
LMA_82	1.3	0.33	1.98	19.31	29.52	0.04	0.09	0.01	0.09	0.37	<0.002	12	29	<1	16.6
LMA_94	2.75	0.78	2.61	18.18	29.26	0.06	0.17	0.03	0.08	0.41	<0.002	19	32	<1	15.3
LMA_300	38.91	3.21	2.22	10.79	17.02	0.03	1.27	0.18	0.34	0.17	0.004	59	<20	3	15.6
LMA_310	8.75	1.66	1.33	18.01	26.81	0.02	0.68	0.08	0.05	0.14	<0.002	41	<20	2	12.2
LMA_311	2.12	0.32	1.72	19.17	29.44	0.03	0.1	0.02	0.06	0.24	<0.002	17	33	<1	16.5
ARR_12	16.03	1.72	1.5	16.35	24.87	0.03	0.52	0.11	0.11	0.04	0.002	125	35	2	18.4
ARR_29	12.7	1.69	1.13	17.31	25.94	0.03	0.43	0.09	0.07	0.04	0.003	115	33	2	10.2
ARR_49	4.84	0.71	0.99	19.31	28.6	0.12	0.12	0.04	0.02	0.05	<0.002	22	29	<1	14.9
ARR_77	4.43	0.65	0.92	19.15	28.97	0.02	0.2	0.03	0.02	0.05	<0.002	61	29	<1	15.2
ARR_101	8.11	0.85	1.57	18.64	27.22	0.02	0.3	0.05	0.06	0.14	<0.002	38	<20	<1	12.7
ARR_127	1.75	0.89	1.52	19.73	28.8	0.02	0.17	0.07	0.09	0.27	0.002	22	29	<1	16.3
CLI_1	42.04	9.29	3.96	1.86	20.38	1.48	1.58	0.52	0.53	0.26	0.01	330	<20	9	7.9

samples	Sum	Be ppm	Co ppm	Cs ppm	Ga ppm	Hf ppm	Nb ppm	Rb ppm	Sn ppm	Sr ppm	Ta ppm	Th ppm	U ppm	V ppm
ABE 9_2	99.66	<1	0.5	0.2	<0.5	0.3	0.3	2.3	<1	26009.8	<0.1	0.4	1	<8
ABE9_3	99.82	<1	0.6	0.2	<0.5	0.4	0.3	2.3	<1	1277	<0.1	0.4	0.8	<8
ABE9_4	99.73	<1	0.5	0.3	<0.5	0.2	0.3	2.7	<1	2111.2	<0.1	0.4	0.9	<8
ABE9_5	99.8	<1	0.8	0.3	<0.5	0.3	0.4	3.3	<1	1495.9	<0.1	0.5	1.1	9
PAS_2	99.82	<1	2.4	1	2.9	1.5	1.9	15.1	<1	1108.7	0.1	1.8	2.7	25
PAS_3	99.82	<1	2.3	0.7	1.32	1.1	1.4	9.1	<1	1133.1	0.1	1.5	2.7	20
PAS_8	99.74	<1	1.1	0.6	1.1	2	1.9	6.9	<1	1750.9	0.1	1.6	2.9	14
IBOR_1b	99.82	<1	1.9	0.7	2.2	0.7	1.7	17.8	<1	1139.5	0.1	1.4	2.2	30
IBOR_1d	99.81	<1	1.7	0.6	1.5	0.7	1.5	14.3	<1	1292.9	0.1	1.4	2	22
IBOR_4b	99.42	<1	1.2	<0.1	<0.5	0.9	0.2	1.2	<1	12.5	<0.1	0.4	0.7	<8
IBOR_4c	99.59	<1	2.2	0.7	2	1.1	1.7	12.5	<1	41.7	0.1	1.9	0.8	12
LMA-2A	99.92	<1	1.4	0.5	1.6	1.1	1.5	10.9	<1	220.7	<0.1	1.5	4.8	24
LMA_8	99.87	<1	2	0.3	1.8	1.4	1.7	10.7	<1	441.7	0.1	1.8	3.5	16
LMA_82	99.64	<1	1	0.1	<0.5	0.1	0.2	2.4	<1	99.4	<0.1	0.5	0.6	<8
LMA_94	99.66	<1	4.5	0.4	<0.5	1	0.4	4.7	<1	62.7	<.1	0.9	1.9	<8
LMA_300	99.78	<1	1.5	0.7	3.9	2.5	2.4	17.9	2	27.8	0.2	3.8	3	25
LMA_310	99.69	<1	2	0.7	1.2	0.7	0.8	10	<1	9.8	<0.1	1.1	2.2	15
LMA_311	99.67	<1	0.6	<0.1	<0.5	1	0.2	2.4	<1	14.3	<0.1	0.3	1.1	<8
ARR_12	99.7	<1	1.4	0.6	0.8	1.6	1.5	14.9	<1	79.1	0.1	1.5	1.5	15
ARR_29	99.68	<1	1.5	0.6	1.1	0.9	1.1	13.5	<1	90.3	<0.1	1.6	0.7	23
ARR_49	99.66	<1	0.7	0.2	<0.5	0.4	0.6	3	<1	79.6	0.1	1.1	1.2	<8
ARR_77	99.66	<1	6	0.1	<0.5	0.4	0.4	5.3	<1	87.3	<0.1	0.4	1.2	<8
ARR_101	99.67	<1	0.9	0.3	0.7	0.4	0.5	7.4	<1	36	<0.1	0.6	1	10
ARR_127	99.65	<1	1.2	0.2	0.8	1	0.9	4.6	<1	31.3	<0.1	1.6	0.05	<8
CLI_1	99.87	<1	10.4	2.4	11.3	3.3	7.2	56	2	319.5	0.6	6.1	2.3	62

samples	W ppm	Zr ppm	Y ppm	La ppm	Ce ppm	Pr ppm	Nd ppm	Sm ppm	Eu ppm	Gd ppm	Tb ppm	Dy ppm	Ho ppm	Er ppm	Tm ppm
ABE 9_2	<0.5	11.3	5.3	2	4.1	0.51	1.9	0.47	0.12	0.62	0.09	0.53	0.12	0.35	0.05
ABE9_3	2.2	16.7	6.3	2.3	4.8	0.58	2.7	0.64	0.2	0.67	0.11	0.75	0.14	0.41	0.05
ABE9_4	<0.5	8	5.6	2.2	5.4	0.58	2.5	0.54	0.14	0.71	0.1	0.67	0.14	0.4	0.04
ABE9_5	1	12.1	6.3	2.5	4.9	0.58	2.4	0.56	0.14	0.81	0.11	0.74	0.14	0.41	0.05
PAS_2	<0.5	63.8	13.9	14.2	29.9	3.27	12.8	2.63	0.74	2.49	0.37	2.3	0.47	1.19	0.17
PAS_3	0.7	45.6	7.6	8.1	15.2	1.71	6.6	1.23	0.35	1.32	0.19	1.19	0.26	0.72	0.08
PAS_8	0.8	82	17.3	7.9	19.3	2.02	8.7	2.34	0.8	2.99	0.48	2.87	0.52	1.57	0.19
IBOR_1b	<0.5	30.2	6.5	7.8	14.5	1.73	6.8	1.27	0.38	1.3	0.18	1.09	0.22	0.63	0.08
IBOR_1d	<0.5	23.4	6.3	7.5	14.1	1.66	6.5	1.27	0.36	1.23	0.17	0.93	0.19	0.58	0.07
IBOR_4b	<0.5	40.4	4.1	1.3	2.8	0.49	2.6	0.73	0.2	0.82	0.13	0.78	0.15	0.38	0.04
IBOR_4c	<0.5	48.2	8.7	10	20	2.42	10	1.88	0.44	2.08	0.27	1.49	0.26	0.76	0.09
LMA-2A	<0.5	46.2	9.8	9.6	19.3	2.19	9.1	1.79	0.52	1.85	0.25	1.53	0.29	0.84	0.1
LMA_8	0.5	61.3	12.9	11	21.6	2.42	9.4	1.98	0.67	2.2	0.32	1.91	0.37	1.01	0.12
LMA_82	<0.5	6.6	6.5	7.5	15.5	2.18	9.7	1.81	0.4	1.66	0.2	1.12	0.19	0.45	0.05
LMA_94	<0.5	48.7	8	9.7	17.9	2.47	10.6	2.44	0.68	2.39	0.3	1.57	0.27	0.63	0.08
LMA_300	<0.5	95.5	18.7	15.8	36.1	3.74	15.1	3.21	0.78	3.36	0.49	2.97	0.58	1.58	0.23
LMA_310	<0.5	26.5	5.1	3.4	7.3	0.94	3.8	0.79	0.35	0.91	0.15	0.81	0.19	0.45	0.07
LMA_311	0.7	37.1	2.1	2.1	4.3	0.4	1.6	0.3	0.11	0.4	0.05	0.35	0.07	0.17	0.01
ARR_12	<0.5	67.1	11.4	9.9	27.9	2.7	11	2.34	0.65	2.37	0.34	1.99	0.36	0.95	0.11
ARR_29	<0.5	37	8	8.4	26.2	2.19	9.1	1.96	0.4	1.85	0.25	1.58	0.3	0.76	0.09
ARR_49	<0.5	17.4	7	7.9	26	1.81	7.1	1.49	0.34	1.63	0.22	1.39	0.2	0.64	0.07
ARR_77	<0.5	15	2.7	3.5	6.8	0.63	2.7	0.53	0.13	0.59	0.07	0.4	0.08	0.27	0.02
ARR_101	0.5	17.5	7.8	6.8	18.5	1.78	7	1.34	0.39	1.54	0.24	1.41	0.27	0.65	0.12
ARR_127	1.3	38.8	17.3	10.4	34.3	2.64	10.5	2.5	0.74	3.06	0.47	2.94	0.6	1.72	0.2
CLI_1	1.1	122.1	25.9	25	49.1	5.73	22.4	4.75	1.07	4.25	0.7	3.9	0.9	2.43	0.37

samples	Yb ppm	Lu ppm	Mo ppm	Cu ppm	Pb ppm	Zn ppm	Ni ppm	As ppm	Cd ppm	Sb ppm	Bi ppm	Ag ppm	Au ppm	Hg ppm
ABE 9_2	0.3	0.05	0.1	1.9	17.1	32	0.3	0.6	<0.1	0.4	<0.1	<0.1	<0.5	0.12
ABE9_3	0.36	0.05	0.1	1.7	6.6	13	1	0.9	<0.1	0.3	<0.1	<0.1	1	0.05
ABE9_4	0.29	0.04	<0.1	1.2	3.8	6	0.3	<0.5	<0.1	0.5	<0.1	<0.5	0.05	
ABE9_5	0.36	0.05	<0.1	1.6	5.3	9	1.2	1.4	<0.1	1.9	<0.1	<0.1	0.9	0.06
PAS_2	1.05	0.14	0.3	5.6	8.2	24	6	4.8	<0.1	0.4	<0.1	<0.1	0.7	<0.01
PAS_3	0.57	0.08	0.6	5	6.3	23	5	1.7	<0.1	0.2	<0.1	<0.1	<0.5	<0.01
PAS_8	1.16	0.15	0.2	2.3	8	20	2.5	1.1	<0.1	0.1	<0.1	<0.1	<0.5	<0.01
IBOR_1b	0.54	0.07	0.3	4.9	4.5	13	4.5	1.5	0.1	<0.1	<0.1	<0.1	<0.5	0.04
IBOR_1d	0.48	0.06	0.2	4.1	3.1	10	3	0.9	<0.1	<0.1	<0.1	<0.1	<0.5	0.004
IBOR_4b	0.25	0.03	<0.1	1.3	2.2	2	1.2	0.9	<0.1	0.2	<0.1	<0.1	<0.5	0.02
IBOR_4c	0.64	0.08	<0.1	3.6	1.9	7	3.7	0.6	<0.1	<0.1	<0.1	<0.1	<0.5	0.01
LMA-2A	0.67	0.09	0.2	3.9	3.7	9	2.9	2.7	<0.1	0.2	<0.1	<0.1	<0.5	0.002
LMA_8	0.85	0.11	0.6	2.8	4.6	28	3.6	6.7	0.1	0.5	<0.1	<0.1	<0.5	0.03
LMA_82	0.31	0.03	0.2	1.6	11.8	40	1.4	<0.5	0.1	0.1	<0.1	<0.1	<0.5	0.02
LMA_94	0.4	0.05	<0.1	5.3	5.8	17	3	1.7	<0.1	0.2	<0.1	<0.1	<0.5	0.04
LMA_300	1.41	0.24	0.1	2.3	12.4	100	4.3	1.4	0.4	0.2	<0.1	<0.1	<0.5	0.06
LMA_310	0.41	0.07	<0.1	2.8	4.3	23	3.7	1.6	<0.1	0.1	<0.1	<0.1	<0.5	0.01
LMA_311	0.17	0.02	<0.1	2.4	2.6	8	0.4	<0.5	<0.1	<0.1	<0.1	<0.1	<0.5	0.01
ARR_12	0.73	0.1	0.2	1.6	5.5	12	2.8	1.9	<0.1	0.1	<0.1	<0.1	<0.5	<0.01
ARR_29	0.61	0.08	<0.1	2	11	28	3.7	<0.5	0.4	<0.1	<0.1	<0.1	<0.5	<0.01
ARR_49	0.46	0.05	0.2	0.9	5.7	11	1.1	0.7	<0.1	<0.1	<0.1	<0.1	<0.5	0.02
ARR_77	0.18	0.03	<0.1	1.1	3.8	10	1.3	0.7	<0.1	<0.1	<0.1	<0.1	<0.5	<0.01
ARR_101	0.59	0.09	0.6	2.5	7	25	2.1	4.6	<0.1	<0.1	<0.1	<0.1	<0.5	<0.01
ARR_127	1.21	0.18	<0.1	1.3	2.5	17	1.1	<0.5	0.1	<0.1	<0.1	<0.1	<0.5	<0.1
CLI_1	2.32	0.33	0.1	34.5	5.1	54	22	2.9	<0.1	0.7	<0.1	<0.1	0.6	0.01